Initial Evaluation of Spoiled Transmit Beam Operations on the Advanced Technology Demonstrator

Technical Report

prepared by: **Rakshith Jagannath, Feng Nai, Christopher Curtis, and Sebastian Torres**

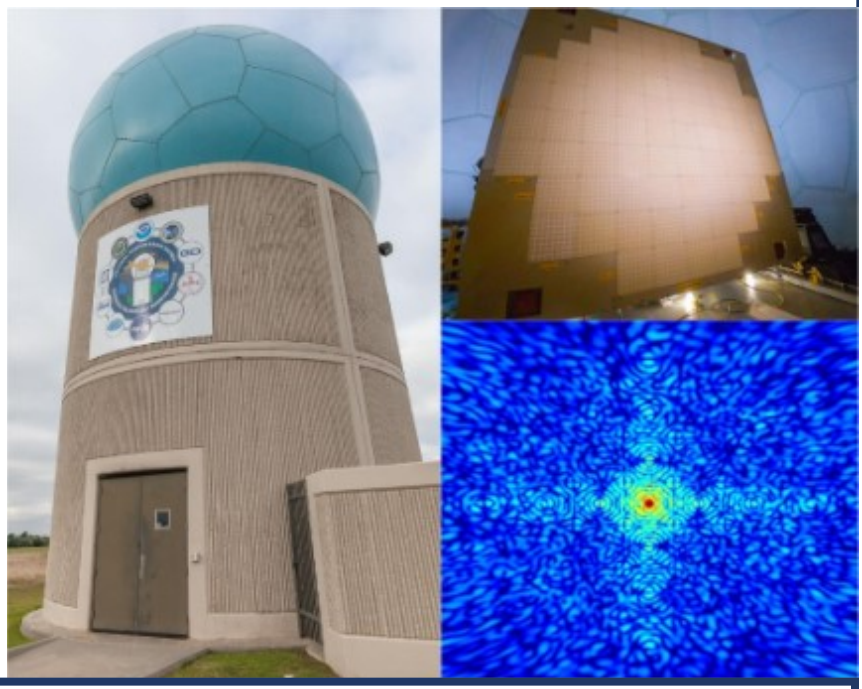

May 2025

Cooperative Institute for Severe and High-Impact Weather Research and Operations
The University of Oklahoma

National Severe Storms Laboratory
National Oceanic and Atmospheric Administration

Contents

Chapter 1

Introduction

The ability to collect good-quality data with rapid updates is one of the most important features for weather radars. This helps the forecasters by improving their visualization of the formation and evolution of large and small scale weather phenomena. Consequently, the warning lead time, situational awareness, and the confidence level in their warning decisions are all improved.

Phased array radars (PARs) are one of the best tools for obtaining rapid updates. PARs provide rapid updates through their ability to electronically form and steer directional electromagnetic radiations (also called beams) to any required direction. Conventional weather radars, such as the Weather Surveillance Doppler Radar (WSR-88D), produce beams that are steered mechanically by rotating the antennas to the required direction. In contrast, this steering is done in PARs by high-speed electronic circuits, which allows for the ability to change steering directions almost instantaneously. Hence, PARs are able to provide faster updates by a combination of fast electronic steering and more agile beamforming.

Another way to reduce scan times in a PAR is transmit beam spoiling (simply referred to as beam spoiling). In this technique, the transmit beam is intentionally broadened so that the main lobe is wider than that of a typical operational beam (simply referred to as a pencil beam). On receive, digital beamforming is employed to form multiple simultaneous receive pencil beams to sample the volume illuminated by the broadened transmit-beam main lobe. This simultaneous sampling

of the space reduces the scan time, resulting in rapid updates.

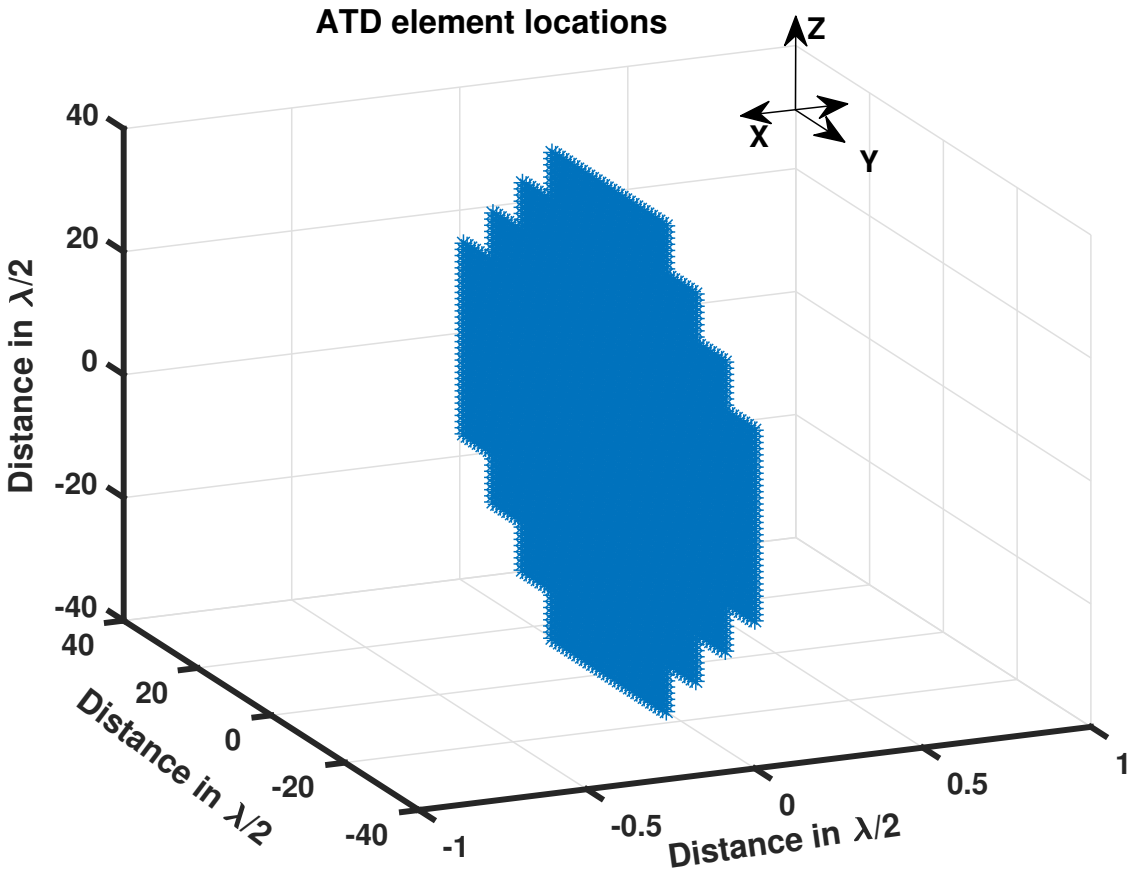

Figure 1.1: ATD element locations.

The Advanced Technology Demonstrator (ATD) is the first full-scale, S-band, dual-polarization phased array radar. The ATD has a flat, or planar, antenna composed of 76 panels with $4,864$ radiating elements as shown in Figure 1.1. Using these elements, the ATD produces narrow "pencil" beams for weather measurements. The ATD pencil beams have been leveraged to evaluate scanning strategies with volumetric update time of about minute and with update time of about 30 seconds for $0.5°$ elevations.

To achieve faster volumetric update rates, the ATD can use beam spoiling (Palmer et al., 2022; Schvartzman et al., 2021). The spoiled beam capability for ATD was implemented in the fall of 2023 for engineering evaluation. With the current implementation, the ATD can spoil the transmit beams in azimuth by a spoil factor of 3 or 5, illuminating an area three or five times that of the

ATD pencil beams. On receive, digital beamforming is employed to form multiple simultaneous receive pencil beams within the geometry of the broadened transmit beam main lobe. The ATD can currently provide 3, 5 or 9 simultaneous receive beams for sampling the area illuminated by the transmit beam.

Chapter 2

Background

The ATD makes weather observations using predefined scan strategies (simply referred to as a scan) that are defined by radar operators. In a typical scan, the ATD sequentially illuminates a region of interest with its transmit beam and samples the echoes from the illuminated region with a corresponding receive beam. Generally, two scan techniques, the plan position indicator (PPI) scan and the range height indicator (RHI) scan, are used in the ATD, although mixed scan modes are also possible. A PPI scan is a collection of elevation cuts. For each elevation cut, the elevation is fixed and the ATD sequentially scans electronically over different azimuths. An RHI scan is a collection of azimuth slices. For each azimuth slice, the azimuth is fixed and the ATD sequentially scans electronically over different elevations. It is assumed that the dominant echoes from the hydrometeors arrive from the resolution volume, V_6, that is defined by the 6 dB contours of the range weighting function and the two-way antenna pattern.

The ATD illuminates a region in the atmosphere by producing a transmit beam and pointing it in the appropriate direction. The ATD transmit beam is steered to an azimuth angle ϕ_0 and elevation angle θ_0 by applying complex weights, $\alpha_n, n = 1, 2, \ldots, N = 4864$ to each of the radiating elements. For example, the transmit beam pattern for an ATD beam steered to the location (ϕ_0, θ_0) is given by,

$$\mathbf{A}_{Tx}(\phi, \theta) = \mathbf{A}^{e}_{Tx}(\phi, \theta) \sum_{n=1}^{N} \alpha_n(\phi_0, \theta_0) \exp\left(j \frac{2\pi}{\lambda} \mathbf{p}_n^T \mathbf{k}(\phi, \theta)\right), \tag{2.1}$$

where $\mathbf{A}_{Tx}^{e}$ is the transmit element pattern, and we use the coordinate system from (Ivić, 2023). ϕ and θ used here and throughout the report are "phase-relative" angles unless mentioned otherwise. Furthermore, we use azimuth and ϕ interchangeably and we use elevation El to denote the phase relative angle $90^{\circ} - \theta$. In equation (2.1), the element patterns for all the ATD elements are assumed to be exactly the same. The location of the nth element in the $y - z$ plane is given by $\mathbf{p}_n = [y_n, z_n]$ and $\mathbf{k}(\phi, \theta) = [\sin(\theta)\sin(\phi), \cos(\theta)]$ is the wave vector. The complex weights used to steer the transmit beam to (ϕ_0, θ_0) are obtained by, $\alpha_n(\phi_0, \theta_0) = \alpha_n(0,0)\exp\left(-j\frac{2\pi}{\lambda}\mathbf{p}_n^T\mathbf{k}(\phi_0, \theta_0)\right)$, where $\alpha_n(0,0)$ is the broadside taper stored in the beam steering generator (BSG) sub-system of the ATD. In general, phase-only tapers ($|\alpha_n(0,0)| = 1, \forall n$) are used to maintain constant maximum transmit power. In equation (2.1), the weighted sum of the radiation from all the ATD elements produces a directional ATD transmit beam pointing to (ϕ_0, θ_0), with the tapers controlling the properties of the transmit beam.

The ATD samples the region illuminated by the transmit beam using a corresponding receive beam. Hence, the receive beam must point in the direction illuminated by the transmit beam. The ATD receive beam pointing at (ϕ_0, θ_0) is generated by an overlapping sub-array architecture, which is illustrated in Figure 2.1. In the receive mode, the N ATD elements are divided into $N_m = 24$ overlapping subarrays, each consisting of $N_s = 512$ elements (32×16). Each of the N_m sub-arrays produces a wide received beam, pointing at (ϕ_0, θ_0) with radiation given by

$$\mathbf{A}_{Rx}^{s}(\phi, \theta) = \mathbf{A}_{Rx}^{e}(\phi, \theta)\sum_{n=1}^{N_s}\beta_n(\phi_0, \theta_0)\exp\left(j\frac{2\pi}{\lambda}\mathbf{p}_n^T\mathbf{k}(\phi, \theta)\right), \tag{2.2}$$

where, $\beta_n(\phi_0, \theta_0), n = 1, 2, \ldots, N_s$ is the receive sub-array taper of element n and $\mathbf{A}_{Rx}^{e}(\phi, \theta)$ is the receive element pattern. A simulated sub-array beam pointing at broadside $(\phi_0 = 0, \theta_0 = 0)$ is illustrated in Figure 2.2. The receive sub-array taper used to steer the receive beam to (ϕ_0, θ_0) is obtained by $\beta_n(\phi_0, \theta_0) = \beta_n(0,0)\exp\left(-j\frac{2\pi}{\lambda}\mathbf{p}_n^T\mathbf{k}(\phi_0, \theta_0)\right)$, where $\beta_n(0,0)$ is the broadside taper of the element n stored in the BSG. The $N_m = 24$ sub-array beams are further digitally combined using a set of digital beamforming (DBF) weights, $\alpha_s(\Delta\phi_0, \Delta\theta_0)$ to obtain the final receive beam

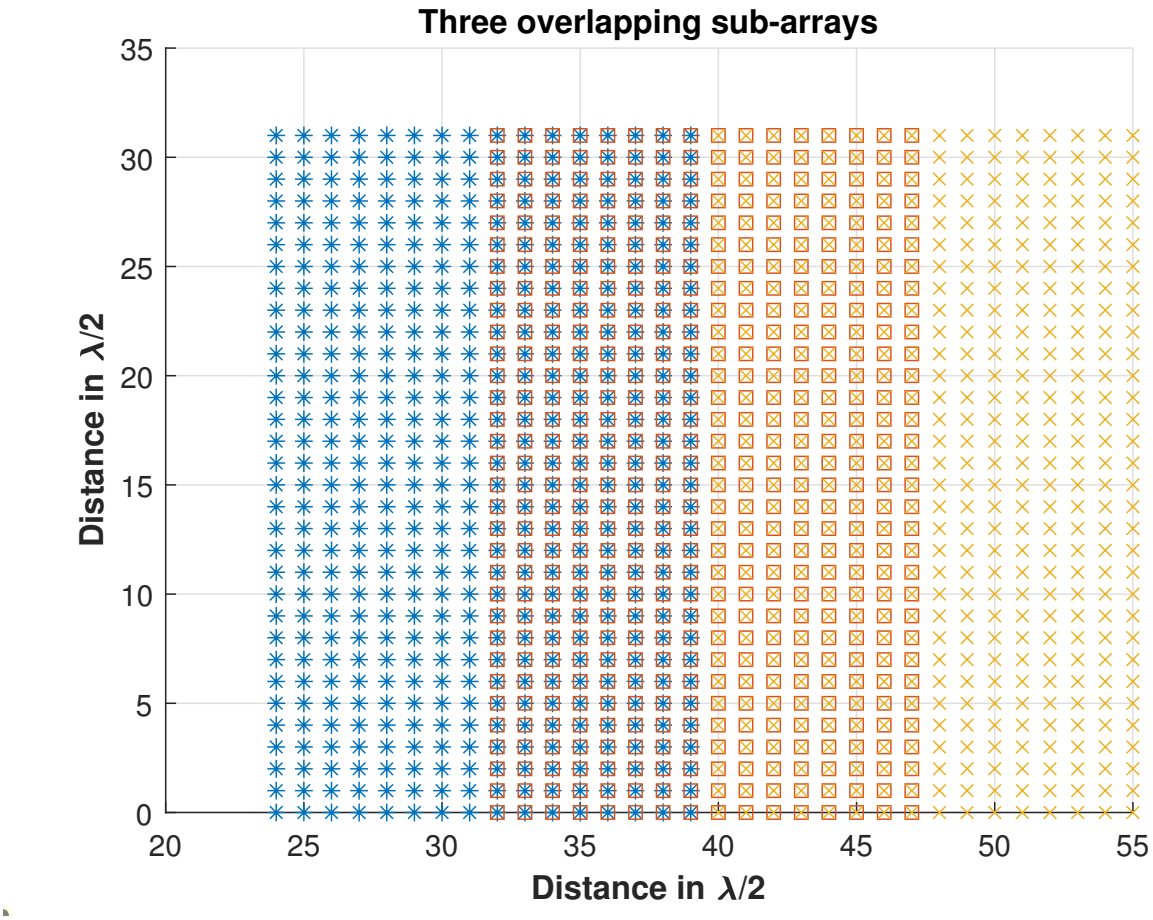

Figure 2.1: Illustration of three overlapping sub-arrays.

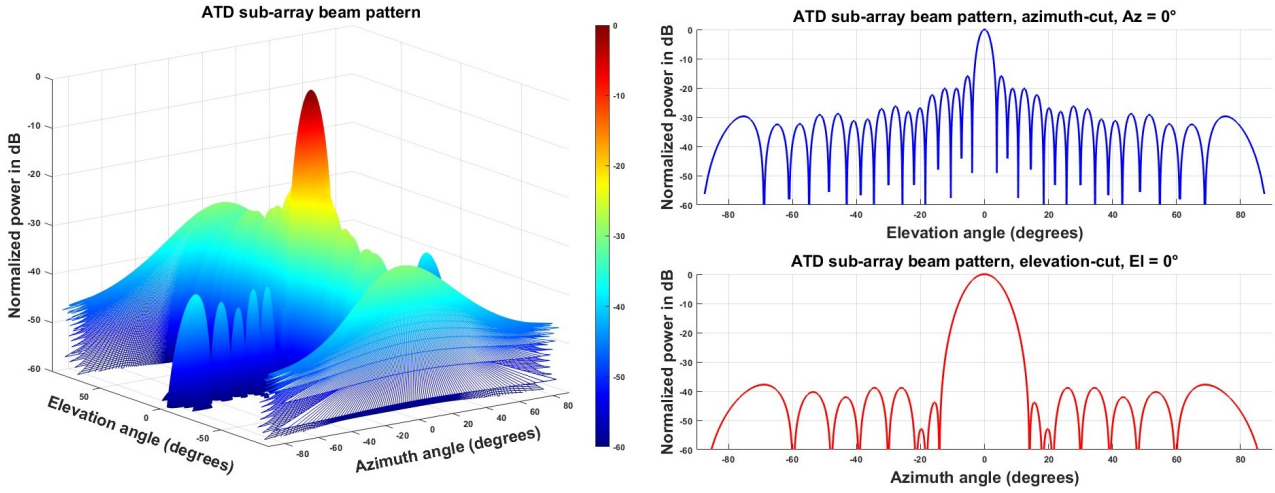

(a) (b)

Figure 2.2: Simulated sub-array beam pattern.

as,

$$\mathbf{A}_{Rx}(\phi,\theta) = \sum_{n=1}^{N_m} \alpha_s(\Delta\phi_0, \Delta\theta_0)\mathbf{A}^s_{Rx}(\phi,\theta). \tag{2.3}$$

More details about the weights $\alpha_s(\Delta\phi_0, \Delta\theta_0)$ are provided in Section 2.2 below. For pencil beam operations, $(\Delta\phi_0 = 0, \Delta\theta_0 = 0)$ ensures that the receive beam points exactly to (ϕ_0, α_0). The received beam produced in equation (2.3) effectively samples the area illuminated by the transmit beam, resulting in a two-way beam given by

$$\mathbf{A}_{Tot}(\phi,\theta) = \mathbf{A}_{Tx}(\phi,\theta) \times \mathbf{A}_{Rx}(\phi,\theta). \tag{2.4}$$

We will now discuss the details of how ATD scans the atmosphere using the transmit, receive and the two-way beams.

2.1 ATD spatial sampling techniques

The scans defined for weather observations require the ATD to observe a wide region of the atmosphere. The smallest region of the atmosphere that can be sampled by the ATD at a particular time is equal to the ATD resolution volume, V_6. The azimuthal dimension of the resolution volume is defined by the azimuthal beamwidth, BW_{Tot}, of the two-way beam pattern. The typical beamwidth of the ATD beam is much smaller than the region of storms being sampled. Hence, we require scanning strategies for sampling larger regions of the atmosphere. A typical ATD scan steers the transmit and receive beams over a set of directions (defined by azimuth and elevation angles either relative to the antenna face or to Earth). The set of transmit locations where the ATD transmit beam illuminates the atmosphere is called the transmit spatial sampling grid (simply referred to as the transmit grid). Similarly, the set of locations where the receive beam samples the transmit beam is called the receive spatial sampling grid (simply referred to as the receive grid). In sine-space sampling, the atmospheric region of interest is typically sampled in a manner to ensure that adjacent radials are $\frac{BW_{Tot}}{2}$ apart as illustrated in Figure 2.3a.

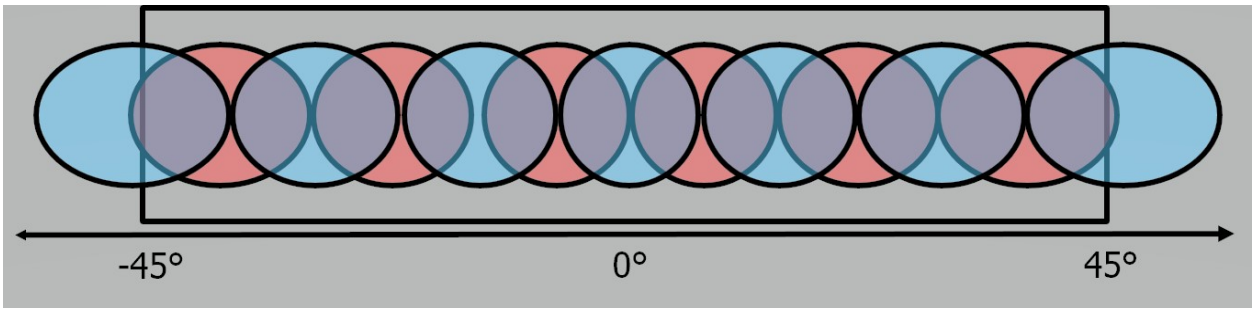

(a) Sine-space sampling

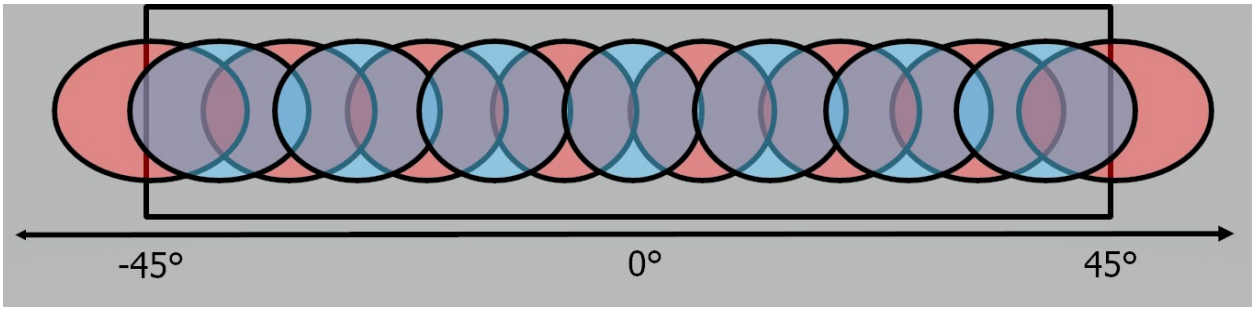

(b) Degree-space sampling

Figure 2.3: Different ATD sampling strategies.

Because the ATD beamwidth varies as the beam is steered away from broadside, the sampling grid locations for sine-space sampling are non-uniform in degrees.

In contrast, for degree-space sampling, the field of view is spatially sampled at fixed degree intervals, which leads to more beam overlap as shown in Figure 2.3b. The degree-space sampling provides a uniform azimuthal grid in degrees. However, using the typical azimuthal sampling spacing of 0.5°, the denser sampling in degree-space leads to more sampling grid positions compared to sine-space sampling.

2.2 ATD beamforming techniques

The ATD has the capacity of producing transmit beams with varying characteristics. As noted in equation (2.1), transmit beams with different properties can be produced by changing the transmit taper. The typical ATD transmit beam is called a pencil beam. It has the narrowest beamwidth (and hence highest spatial resolution) that the ATD can obtain. Azimuthally spoiled transmit beams with spoiling factors of 3 and 5 can also be produced for the purpose of achieving faster updates.

In the following, we describe the ATD pencil beam and spoiled beam properties and their use in operations.

2.2.1 Pencil beam operations

In pencil beam operations, The ATD sequentially transmits a narrow pencil beam pointing over transmit positions pre-defined by a transmit grid. For a PPI scan, the ATD typically scans the region from -45° to 45° azimuth for a fixed elevation. The transmit grid with sine-space sampling and 50% beam overlap that is used for scanning is given by

$$\Gamma_{Tx}^{P,SS}(k) = \sin^{-1}\left(k \sin\left(\frac{BW^P}{2}\right)\right), k = 0, \pm 1, \pm 2, \ldots, \pm L_g, \tag{2.5}$$

where BW^P is the two-way beamwidth of the pencil beam at broadside and $L_g = \lceil \frac{2\sin(45)}{\sin(BW^P)} \rceil - 1$. The number of scan positions with the typical sine-space sampling is $L = 2L_g + 1 = 103$. Similarly, the transmit grid with degree-space sampling and 0.5° spacing is given by

$$\Gamma_{Tx}^{P,DS}(k) = 0.5k, k = 0, \pm 1, \pm 2, \ldots, \pm L_d, \tag{2.6}$$

where $L_d = 90$. The number of scan positions with this type of degree-space sampling is $L = 2L_d + 1 = 181$. The ATD receive beam is in the same direction as the ATD transmit beam. Hence, the receive sampling grid with both sine-space and degree-space sampling is exactly the same as the Tx sampling grid:

$$\Gamma_{Tx}^{P,SS} = \Gamma_{Rx}^{P,SS} \text{ and } \Gamma_{Tx}^{P,DS}(k) = \Gamma_{Rx}^{P,DS}(k). \tag{2.7}$$

The ATD pencil transmit beam, receive pencil beam and two-way pencil beam are illustrated in Figure 2.4. These beams were generated from simulations. The simulation procedure is described in Section 2.5. From the figure, it can be observed that the ATD pencil transmit beam has a 3 dB beamwidth of 1.47°. The ATD receive pencil beam has a 3 dB beamwidth of 1.87°, and the two-way pencil beam has a 6 dB beamwidth of 1.67° with a peak sidelobe level of -48 dB relative to

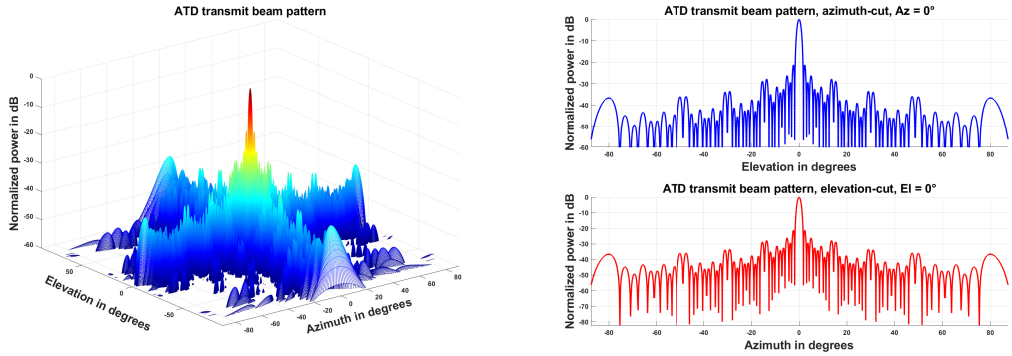

(a) ATD pencil transmit beam.

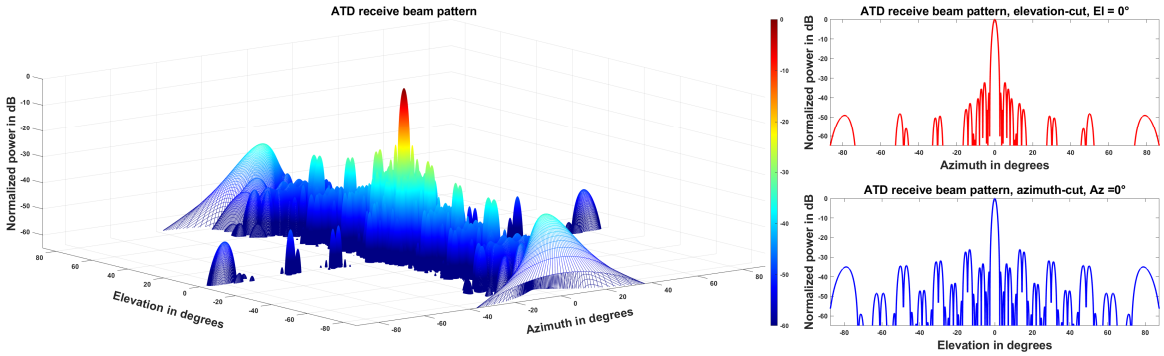

(b) ATD pencil receive beam.

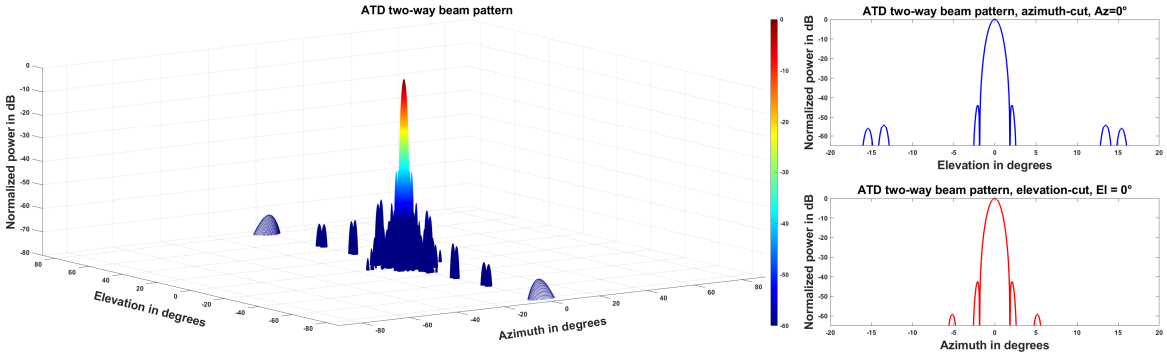

(c) ATD two-way pencil beam.

Figure 2.4: Illustration of ATD transmit beam, receive beam and the two-way beams used in pencil beam operations.

the peak.

2.2.2 Spoiled beam operations

The ATD spoiled beam operations are illustrated in Figure 2.5. The spoil factor, m is defined as the ratio of the beamwidth of the spoiled transmit beam to the beamwidth of the pencil transmit beam.

The ATD currently has the ability to achieve a spoiled factor of $m = 3$ or $m = 5$ in the azimuthal direction. In this work, spoiled beam operations with a spoiled factor of $m = 3$ are studied. The shape of the spoiled transmit beam in elevation is the same as the pencil transmit beam. So, the beamwidth of the spoiled transmit beam in elevation is the same as the pencil transmit beam.

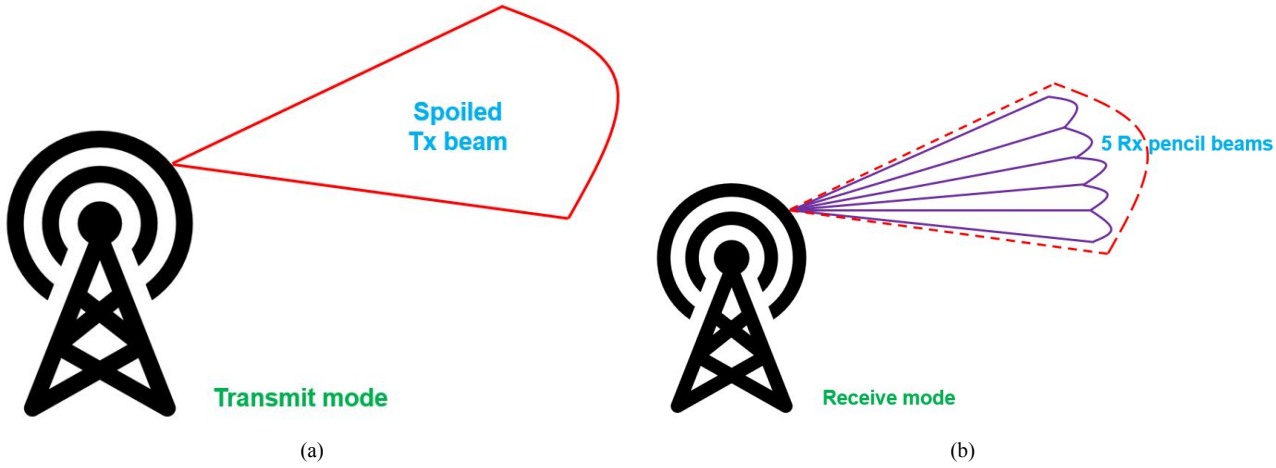

Figure 2.5: Illustration of ATD spoiled beam operations.

On receive, the weather echoes produced from the area illuminated by the spoiled transmit beam are sampled by n simultaneous receive pencil beams. Hence, the update rate increases by a factor of n for spoiled $m \times n$ operations. For a spoiled factor of m, the number of receive beams n is determined by the desired grid spacing. For a degree-space grid, the system typically uses 0.5° or 1° spacings. For a sine-space grid, the system typically uses no overlap between adjacent beams or 50% overlap. For example, for a sine-space grid with adjacent receive beams with 50% overlap and $m = 3$, five receive pencil beams placed at intervals of $BW^p/2$ are used, resulting in the so called "spoiled 3×5" mode of operation. The process of generating the n=5 simultaneous receive beams from the sub-array beams involves simultaneously combining the sub-array beams using a set of DBF weights. The $n = 5$ simultaneous receive beams are pointed to the same elevation as the spoiled transmit beam. Each of the $n = 5$ receive beams are pointed $BW^p/2$ apart with the central receive beam pointing in the same direction as the transmit beam; hence, a set of $n = 5$ DBF weights $\alpha_{s,k}\left(\Delta\phi_k = kBW^p/2, 0\right), k = -2, -1, 0, 1, 2, s = 1, 2, \ldots, 24$ are used to combine the sub-array beams to produce the $n = 5$ receive beams. These weights are also stored in the

DBF (Digital Beam Former) of the backend sub-system and are different for the sine-space and degree-space sampling grids.

The sampling grid for the ATD spoiled transmit beam with sine-space sampling and 50% beam overlap to sample the region between $-45^{\circ} \leq \phi \leq 45^{\circ}$ is given by

$$\Gamma_{Tx}^{Sp,SS}(k) = \sin^{-1}\left(k \sin\left(BW^{p}\frac{\pi}{180}\right)(n-0.5)\right), k = 0, \pm 1, \ldots, L_u = 10. \tag{2.8}$$

The number of scan positions for the spoiled transmit beam with sine-space sampling is $L_{Sp,SS} = 2L_u + 1 = 21$. Similarly, the transmit grid in degree-space with 0.5° spacing is given by

$$\Gamma_{Tx}^{Sp,DS}(k) = k(n-0.5), k = 0, \pm 1, \pm 2, \ldots, \pm L_v = 18. \tag{2.9}$$

The number of scan positions for the spoiled transmit beam with degree-space sampling is $L_{Sp,SS} = 2L_v + 1 = 37$. We note that the number of transmit directions for the spoiled beams with spoiled factor $m = 3$ is reduced compared to pencil beam operations. The receive pencil beams for spoiled beam operations are generated on the sampling grid given by

$$\Gamma_{Rx}^{Sp,SS}(k) = \sin^{-1}\left(k \sin\left(BW^{p}\right)/2\right), k = 0, \pm 1, \pm 2, \ldots, \pm \tilde{L}_g, \tag{2.10}$$

where $\tilde{L}_g = \left\lceil \frac{2\sin(45)}{\sin(BW^{p})} \right\rceil$. The number of sampling locations in sine-space is $M_{Sp,SS} = 2\tilde{L}_g + 1 = 105$. We note that the receive grid for the spoiled beam operations has two additional positions compared to the receive grid for pencil beam operations. Similarly, for degree-space sampling the receive grid is given by

$$\Gamma_{Rx}^{Sp,DS}(k) = 0.5k, k = 0, \pm 1, \pm 2, \ldots, \pm \tilde{L}_v = 92. \tag{2.11}$$

Hence, the number of sampling locations in degree-space is $M_{Sp,DS} = 2\tilde{L}_v + 1 = 185$.

2.3 Performance Considerations

In order to evaluate the performance of the spoiled beam operations, we measure the spoiled beam patterns using the ATD calibration tower (cal-tower) and an external tower. The details of the measurement setup are discussed in Section 2.4. We simulate the theoretical spoiled beam patterns to compare the performance of measured patterns. The simulation setup is discussed in Section 2.5. The performance is compared by evaluating metrics for each pattern. We will compare the peak power, the half-power beamwidth, integrated main-lobe level, peak sidelobe level and the integrated sidelobe level for each pattern. The measurements were designed to allow us to compute these metrics. Further details regarding the computation of these metrics for all the beam patterns obtained from simulations and measurements from the cal-tower and external tower are provided in Chapter 3. For sine-space sampling, we compute the metric for 105 beam patterns from pencil beam operations and 105 beam patterns from spoiled beam operations. We have two extra pencil beam operations ($103 + 2$) in order to match the number of spoiled beams for a fair comparison. Similarly for degree-space sampling, we compute the metric for 185 beam patterns from pencil beam operations and 185 beam patterns from spoiled beam operations respectively.

2.4 Measurement setup

One of the main goals of this evaluation is to measure the transmit beam pattern, the receive beam pattern, and the two-way beam pattern for spoiled 3×5 operations and compare them with the theoretical patterns which are obtained through simulations. The pattern measurements are obtained using two measurement setups that are described next.

2.4.1 Measurements using external tower

In this setup, the external tower is treated as a point target located at ($r = 26$ km, $\phi_t = 187.6^{\circ}$, $\theta_t = 0.9^{\circ}$) (”earth relative”). Only two-way pattern measurement is possible with the external

tower. Furthermore, only one-dimensional antenna patterns are measured for a fixed elevation of $\theta_e = 0.9^\circ$. To measure the pattern for a beam steered electronically at $(\phi_e, \theta_e = 0.9^\circ)$, the ATD pedestal is mechanically rotated in the region $\phi_t - \phi_e - 12.6^\circ \leq \phi_m \leq \phi_t - \phi_e + 12.6^\circ$ in 0.1° steps. The mechanical elevation position is maintained at $\theta_m = 0^\circ$. At each mechanical position, a scan with a pencil transmit beam followed by a spoiled transmit beam is used to collect data. For each of the collected scans, the range bins corresponding to the tower location ($r = 26$ km) are isolated. The power from six adjacent range bins is used for averaging. This method allows us to measure 105 two-way beam patterns, for both pencil and spoiled beam operations for all the electronic beam steering angles in the grid $\Gamma_{Rx}^{Sp,SS}$. The measurements obtained using this method have the advantage that they are obtained in the same way weather collection is performed. Furthermore, the data collection can be done using the weather HMI and hence, many of the automated features of the weather HMI can be leveraged. However, the major disadvantage of this method is that the measurements are impacted heavily by the environment, and it is not possible to separately collect and verify the transmit and receive beam patterns. Hence, we also used the calibration tower to obtain pattern measurements.

2.4.2 Measurements using the ATD calibration tower

The ATD calibration tower (cal tower) can be modeled as a point target located at $(\phi_t = 1.3732^\circ, \theta_t = 4.4^\circ)$ ("earth relative"). The cal tower can measure the transmit and receive antenna patterns separately since it has the ability to both transmit signals to the antenna and return signal received from the antenna to the radar receiver.

The transmit pattern is measured in the region $-10^\circ \leq \phi_p \leq 10^\circ$ around the cal tower. For a fixed electronic steering angle (ϕ_e, θ_e), the mechanical rotation (ϕ_m, θ_m) required to measure the

pattern at $(\phi_p, \theta_p = 0.9^\circ)$ is given by a 3-D rotation formula given by (Ivić, 2023):

$$\phi_m = \phi_p + \tan^{-1}\left(\frac{\sin(\theta_e)\sin(\phi_e)}{\sin(\theta_e)\cos(\phi_e)\cos(\phi_m) - \cos(\theta_e)\sin(\theta_m)}\right), \tag{2.12}$$

$$\theta_m = \sin^{-1}\left(\frac{-b + \sqrt{b^2 - 4ac}}{2a}\right) \text{ or } \theta_m = 180^\circ - \sin^{-1}\left(\frac{-b + \sqrt{b^2 - 4ac}}{2a}\right), \tag{2.13}$$

where

$$a = \cos^2(\theta_e) + \sin^2(\theta_e)\cos^2(\phi_e), b = -2\sin(90 - \theta_p)\sin(\theta_e)\cos(\phi_e),$$
$$\text{and } c = \sin^2(90 - \theta_p) - \cos^2(\theta_e).$$

The ATD pedestal is mechanically rotated to (ϕ_m, θ_m). The radar then transmits the signal to the cal tower, and this signal is received by a horn antenna. The received signal is then sent back to the ATD receiver using a co-axial cable connected to channel 49 of the ATD receiver. The IQ samples from channel 49 are then processed to compute the transmit power at each point ϕ_p in order to obtain the transmit pattern.

The ATD receive pattern is also measured in the region $-10^\circ \leq \phi_p \leq 10^\circ$ around the cal tower. Hence, the mechanical position for the receive beams is exactly the same as that of the transmit beam discussed above. A transmit signal is sent to the cal tower using the coaxial cable. The horn antenna in the cal tower then radiates this transmit signal back towards the ATD, which receives this signal. The received IQ samples are then processed to compute the power at each point ϕ_p in order to obtain the receive pattern.

The measurements obtained from the cal tower are less sensitive to the environment than the external tower. Furthermore, the cal tower can be used to separately measure the transmit and the receive patterns. However, this method currently requires the use of the GD HMI and specialized data-collection recipes.

2.5 Simulation setup

The transmit and receive element patterns, $\mathbf{A}^e_{Tx}(\phi,\theta)$, $\mathbf{A}^e_{Rx}(\phi,\theta)$ had been previously measured for the interval $-48^\circ \leq \phi \leq 50^\circ$ and $-6^\circ \leq \phi_p \leq 28^\circ$ with a uniform spacing of 0.25° in azimuth and 0.25° in elevation, respectively. However, in the simulations, the ATD array pattern is evaluated in $u-v$ space to exploit the use of fast Fourier transforms for speedy computations. Hence, a transformation was needed to convert the domain of the measurement patterns from degree-space to $u-v$ space. Furthermore, the array pattern is evaluated over the interval $-1 \leq u,v \leq 1$ with a grid spacing of $1/N_f = 1/2048$ for both u and v domains. This required a two-dimensional interpolation over the interval where data was available. Over the interval where measurement data was not available (example, $-90^\circ < \phi \leq -48^\circ$, $50^\circ \leq \phi < 90^\circ$, all elevations), an extrapolation was used to extend the measurement data. Hence, the transmit and receive element patterns are given as, $\mathbf{A}^e_{Tx}(\phi,\theta), \mathbf{A}^e_{Rx}(\phi,\theta), -1 \leq u,v \leq 1$, with a grid spacing of $1/N_f$. The array pattern is evaluated from the tapers using a 2-D FFT. As discussed in Section 2.2, the transmit and the sub-array tapers for generating the transmit patterns at $(\phi = 0, \theta = 0)$ are stored in the BSG. As the ATD is a 2-D array, the stored tapers are 80×80 matrices with zero entries in the matrix at locations that do not have elements. Hence, only $N = 4864$ of the 6400 entries are non-zero for the transmit tapers. Similarly, only 512 entries are non-zero for sub-array tapers. For a given taper, the corresponding pattern is obtained by taking a N_f-point 2-D FFT. Let $\mathbf{G}$ be the 80×80 matrix containing the broadside taper. Then the corresponding pattern is given by,

$$\mathbf{A}(\phi,\theta) = FFT2(G, N_f, N_f), \tag{2.14}$$

where $FFT2$ denotes the 2-D FFT function. In order to obtain the pattern for another steering location (ϕ_0,θ_0), the broadside taper is phase-shifted as,

$$\mathbf{G}(\phi_0,\theta_0) = \mathbf{G} \odot \exp\left(j\frac{2\pi}{\lambda}\mathbf{Y}\sin(\theta_0)\sin(\phi_0) + \mathbf{Z}\cos(\theta_0)\right), \tag{2.15}$$

where $\mathbf{Y}$ and $\mathbf{Z}$ be 80×80 matrices with the Y and Z coordinates of the ATD elements, $\odot$ represents the element-wise matrix multiplication. The transmit and the sub-array beams are obtained by first phase shifting the tapers to the desired locations on the grid. The sub-array tapers are further phase-shifted by a differential phase as discussed in Section 2.2 to obtain the final receive tapers. The final receive pattern is obtained by taking the FFT over these modified phase tapers. The two-way pattern is obtained by taking the product of the transmit pattern and the receive pattern.

Chapter 3

Performance Evaluation

In this chapter, we evaluate the performance of spoiled beam operations. To this end, we study the ATD element patterns and one-way beam patterns in Section 3.1. In Section 3.2, we also compare the performance of two-way beam patterns using the metrics discussed in Section 2.3.

3.1 Beam patterns

In this section, we present the ATD element patterns and compare the one-way spoiled transmit and receive beam patterns for the broadside and outer edge beams. The ATD element pattern contributes to beamforming and beam steering as discussed in Section 2.2. Hence, a study of the element pattern and one-way spoiled beam patterns will provide additional insights into the metrics evaluated for the two-way spoiled beam patterns.

3.1.1 Element patterns

The measured transmit element pattern is shown in Figure 3.1a. The left panel of Figure 3.1a shows the 2-D transmit element pattern. The right panel shows the transmit element patterns for the $El = (90 - \theta) = 0^{\circ}$ and $El = 0.9^{\circ}$ cuts. These patterns are for a single element. It is assumed that all the $N = 4874$ elements have the same pattern, though we know that this assumption is just

an approximation.

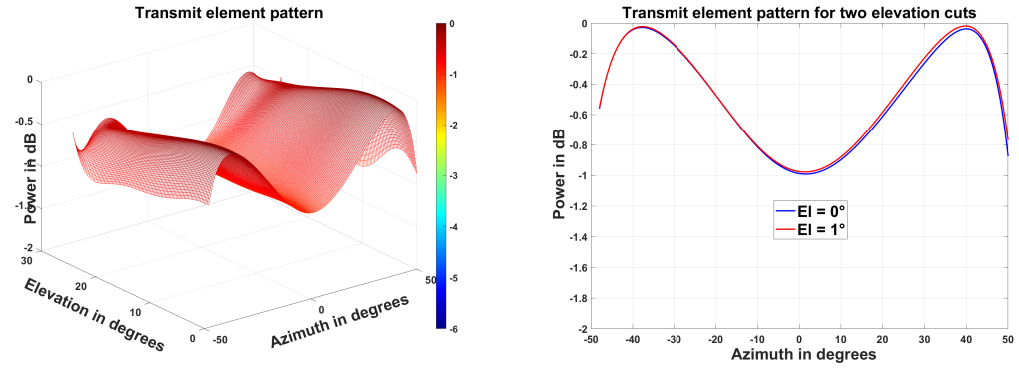

(a) Transmit element pattern.

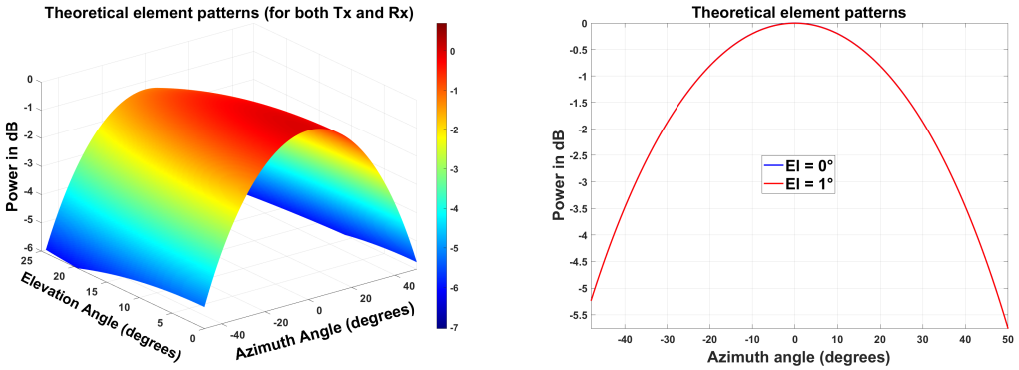

(b) Expected element pattern.

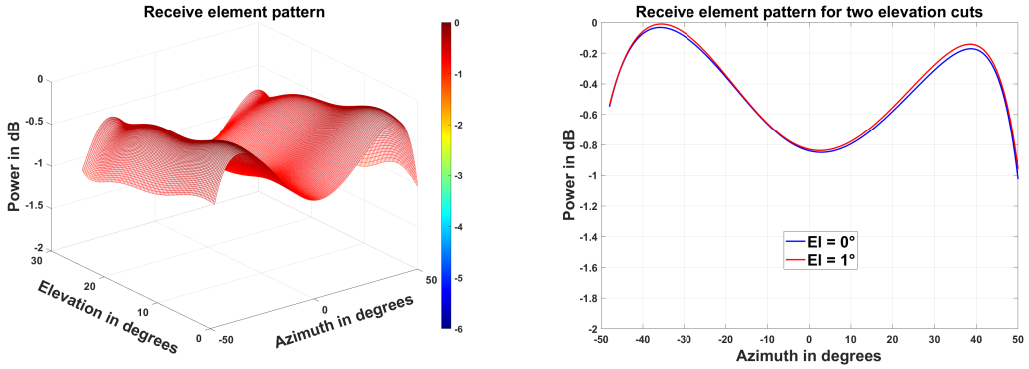

(c) Receive element pattern.

Figure 3.1: ATD element patterns.

For the 2-D pattern, the x-axis represents the azimuth varying over $-48^{\circ} \leq \phi \leq 50^{\circ}$ in steps of 0.25°, the y-axis represents the elevation varying over $0^{\circ} \leq El \leq 25^{\circ}$ in steps of 0.25°, and the z-axis represents the normalized power (normalized by the maximum over all the angles) in dB. For the 1-D patterns, the elevation is constant (different elevations are shown with different colors), the x-axis represents the azimuth as defined above, and the y-axis represents the normalized power in

dB. The ATD elements are rectangular microstrip patch antennas. Hence, the theoretical transmit and receive element patterns are expected to have a flat shape at broadside and a decay at the edges as shown in Figure 3.1b. We make the following observations from Figure 3.1a,

- The 2-D pattern has two ridges. The 2-D pattern obtained from the elevation cut is similar to a sinusoid.
- The patterns have a local minimum close to $\phi = 1.5^{\circ}$, and the normalized power at $\phi = 1.5^{\circ}$ is -1 dB.
- The measured element patterns have smaller power loss for larger steering angles away from broadside compared to the theoretical pattern in Figure 3.1b.

The following inference can be made from the above observations:

- The transmit element pattern from a single element deviates from the expected theoretical patterns.
- The total effect due to the large number ($N = 4874$) of ATD element patterns could be significant in the overall pattern (as will be shown later).

The measured receive element pattern is shown in Figure 3.1c. The left panel of Figure 3.1c shows the 2-D receive element pattern. The right panel shows the receive element patterns for the $El = 0^{\circ}$ and $El = 0.9^{\circ}$ cuts. Again, these patterns are for a single ATD element. The axes for Figure 3.1c are the same as the ones used for the transmit patterns. We make the following observations from Figure 3.1c,

- The receive patterns also have two ridges. Again, the elevation cuts are similar to sinusoids.
- A local minimum normalized power occurs at $\phi = 3.75^{\circ}$, with a value of -0.84 dB.
- The location of the local minima and the ridges are different for the receive element patterns as compared to the transmit element patterns.

The following inferences can be made from the above observations:

- Again, the deviation from the theoretical element pattern from a large number of ATD elements can result in performance that is significantly different from theoretical expectations.
- The transmit and the receive patterns do not have ridges and local minima at exactly the same locations.
- The presence of ridges in the element patterns could result in performance that is significantly different from theoretical expectations when making weather measurements. This will be discussed in the next sections in the context of 2-way patterns.

3.1.2 Spoiled beam patterns

A comparison between the measured and the theoretical beam patterns for the spoiled transmit beam, with three different electronic steering angles for $El = 0.9^{\circ}$, are shown in Figure 3.2. The same comparisons for $El = 0^{\circ}$ are shown in Figure 3.3. The x-axis represents the azimuth varying between $\pm 5^{\circ}$, the y-axis represents the elevation varying between $\pm 1.4^{\circ}$, and the color-scale (and the z-axis for the 3-D mesh plots) represents the normalized power in dB varying over the interval $[0, 6]$ dB. The electronic steering corresponding to each of the plots is shown in the figure title. We make the following observations from Figures 3.2 and 3.3,

- As expected,
  - The spoiled transmit beams are broader in the azimuth direction than in the elevation direction.
  - The span of the beams' ± 6 dB regions are exactly along the expected direction in azimuth.
  - The spoiled transmit beam at 0° azimuth is narrower than the ones at 43.6° azimuth.
- Both the simulated and the measured patterns have saddle points.

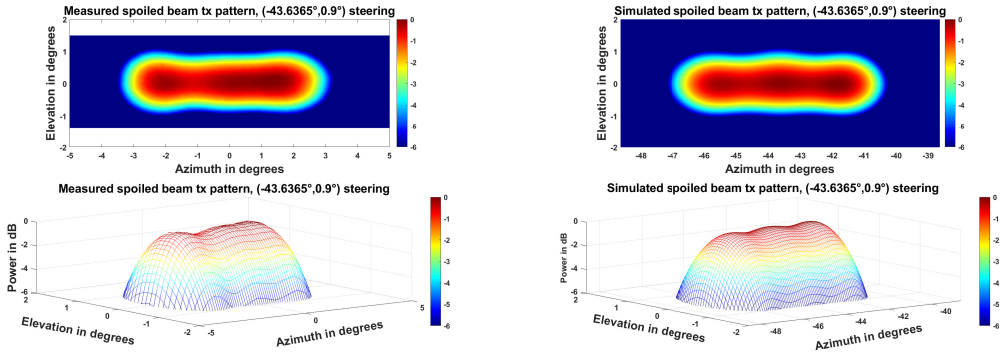

(a) ATD transmit pattern, ($\phi = 43.63^{\circ}$).

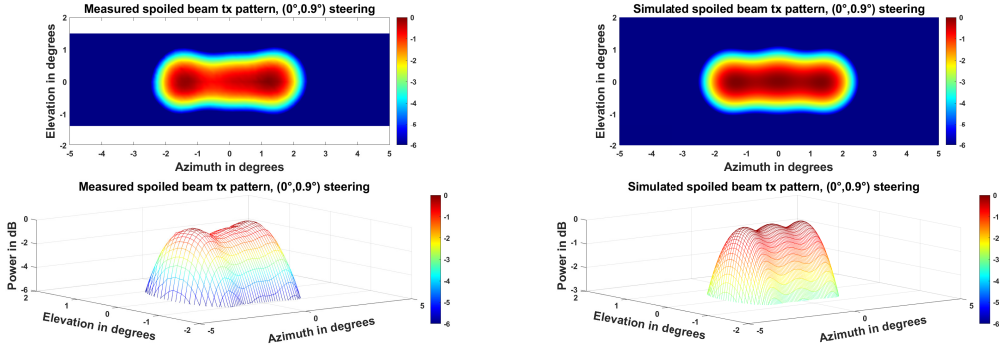

(b) ATD transmit pattern, ($\phi = 0^{\circ}$).

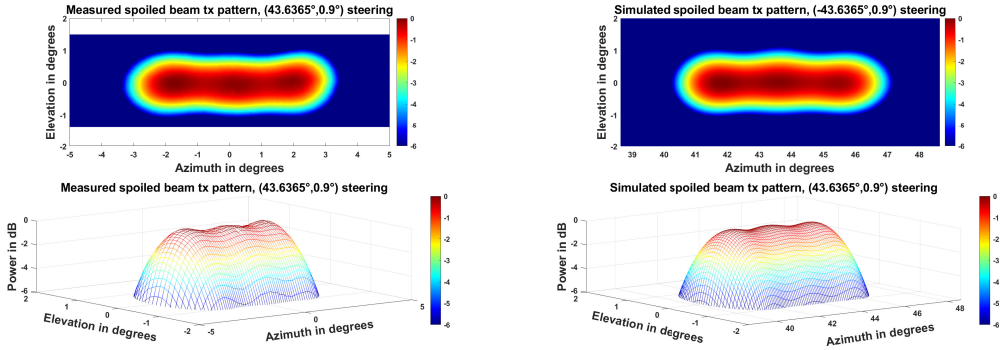

(c) ATD transmit pattern, ($\phi = -43.63^{\circ}$).

Figure 3.2: Comparison of spoiled beam transmit patterns for $El = 0.9^{\circ}$ and different azimuth steering.

- The saddle points in the measured patterns are deeper than those in the theoretical patterns. This is especially clear for the beam pattern corresponding to $(0^{\circ}, 0.9^{\circ})$.
- The depth of the saddle points in the beam patterns varies with the azimuth steering angle.

The following inferences can be made from the above observations:

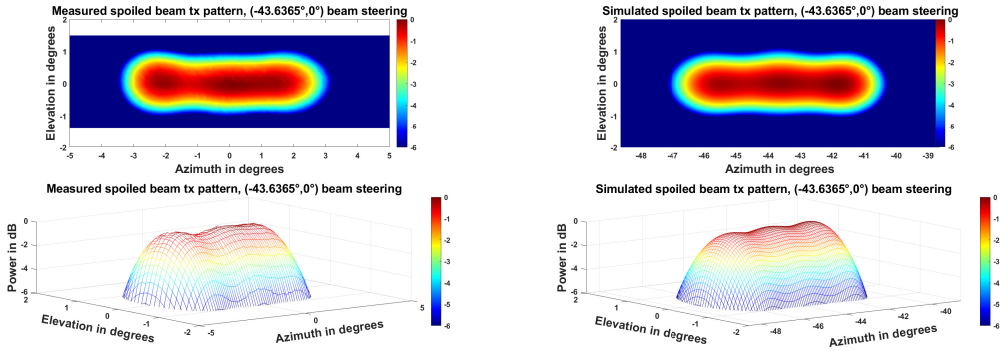

(a) ATD transmit pattern, ($\phi = 43.63^{\circ}$).

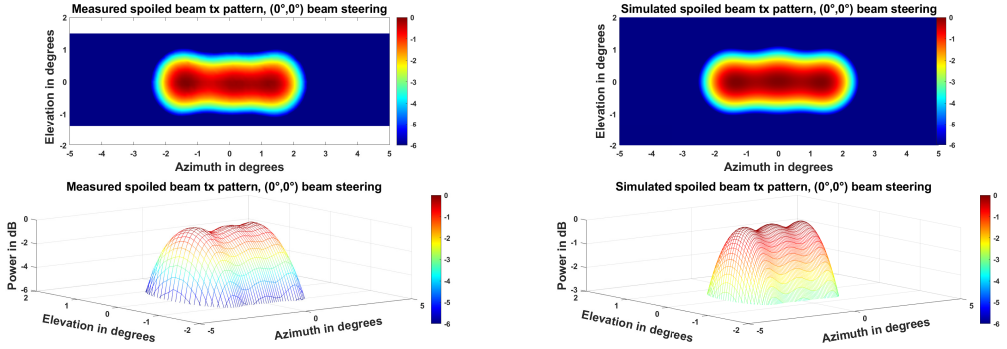

(b) ATD transmit pattern, ($\phi = 0^{\circ}$).

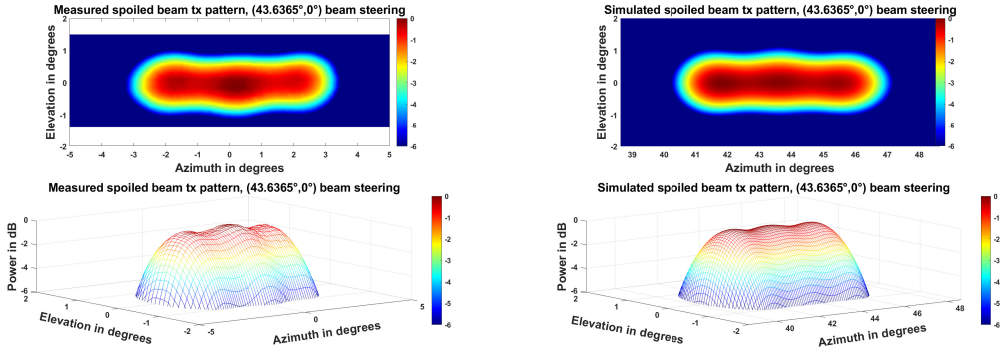

(c) ATD transmit pattern, ($\phi = -43.63^{\circ}$).

Figure 3.3: Comparison of spoiled beam transmit patterns for $El = 0^{\circ}$ and different azimuth steering.

- The ATD produces spoiled transmit beams that appear to be spoiled only in azimuth by a factor close to $m = 3$.
- Furthermore, the transmit beams are steered correctly to the commanded directions.
- The saddle points in the beam patterns could be due to the combined effect of the devia-

tions in the element patterns from the theoretical patterns and other measurement errors and environmental factors.

We define a "receive beam set" as a set of five receive beams that are used to sample a spoiled transmit beam steered in a particular direction (ϕ, El). A comparison between the measured and the theoretical beam patterns for three receive beamsets, corresponding to spoiled transmit beams steered at three different azimuths and a constant $El = 0.9^{\circ}$, is shown in Figure 3.4. The same comparisons for $El = 0^{\circ}$ are shown in Figure 3.5. The top 5 rows show the receive beam set obtained from measurements, and the bottom 5 rows show the same receive beam set obtained through simulations. The spoiled transmit beam's electronic steering in azimuth is $-43.6^{\circ}, 0^{\circ}, 43.6^{\circ}$ for the left, middle, and right columns respectively. The x-axis represents the azimuth relative to the transmit beam's azimuth and varies between $\pm 3^{\circ}$, the y-axis represents the elevation varying between $\pm 2^{\circ}$, and the color scale represents the normalized power in dB varying over the interval $[0, 6]$ dB. We make the following observations from Figures 3.4 and 3.5,

- The receive pencil beams point to the appropriate locations relative to the transmit beams. For example, for the spoiled transmit beam at 0° has a receive beam 1 at $\Delta\phi = 1.6^{\circ}$, a receive beam 2 at $\Delta\phi = 0.8^{\circ}$, a receive beam 3 at $\Delta\phi = 0^{\circ}$, a receive beam 4 at $\Delta\phi = -0.8^{\circ}$, and receive beam 5 at $\Delta\phi = -1.6^{\circ}$.

- The receive pencil beams produced from the spoiled transmit beam at 0° appear to be symmetric. The beams produced at the edges exhibit the expected beam broadening.

- The structure of the receive pencil beams obtained from simulations is very similar to the one obtained from measurements. However, the measured beams are not as smooth as the simulated beams.

The following inferences can be made from the above observations:

- The receive beams have the same main-lobe shape as the pencil beams.

- The receive beams point closely to the expected locations.

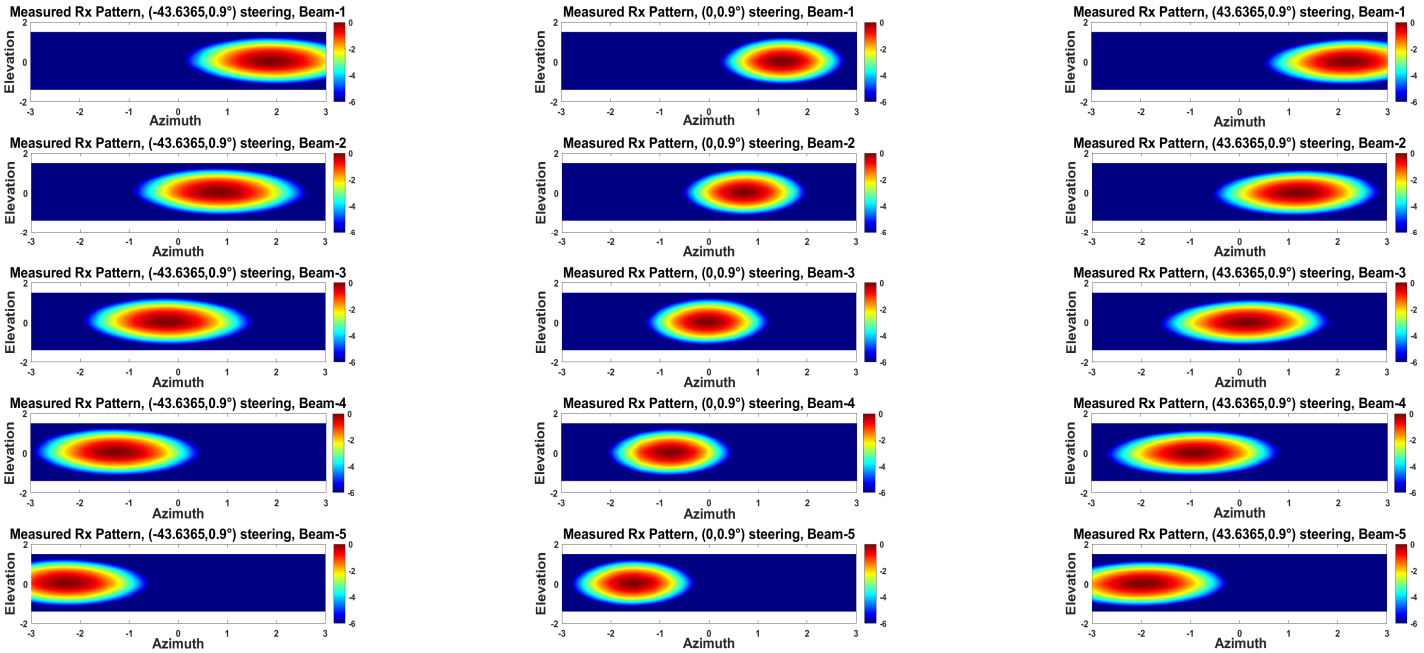

(a) Measured receive patterns.

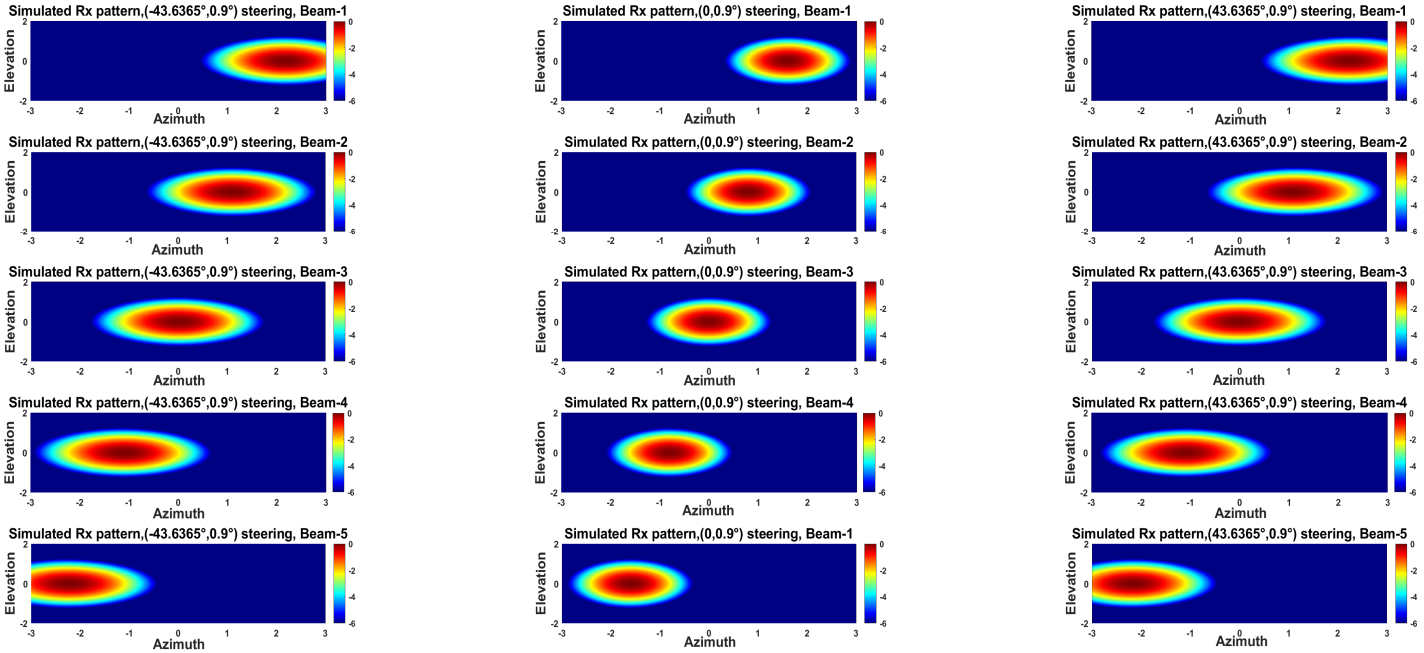

(b) Simulated receive patterns.

Figure 3.4: Comparison of receive pencil beams from spoiled beam operations for $El = 0^{\circ}$.

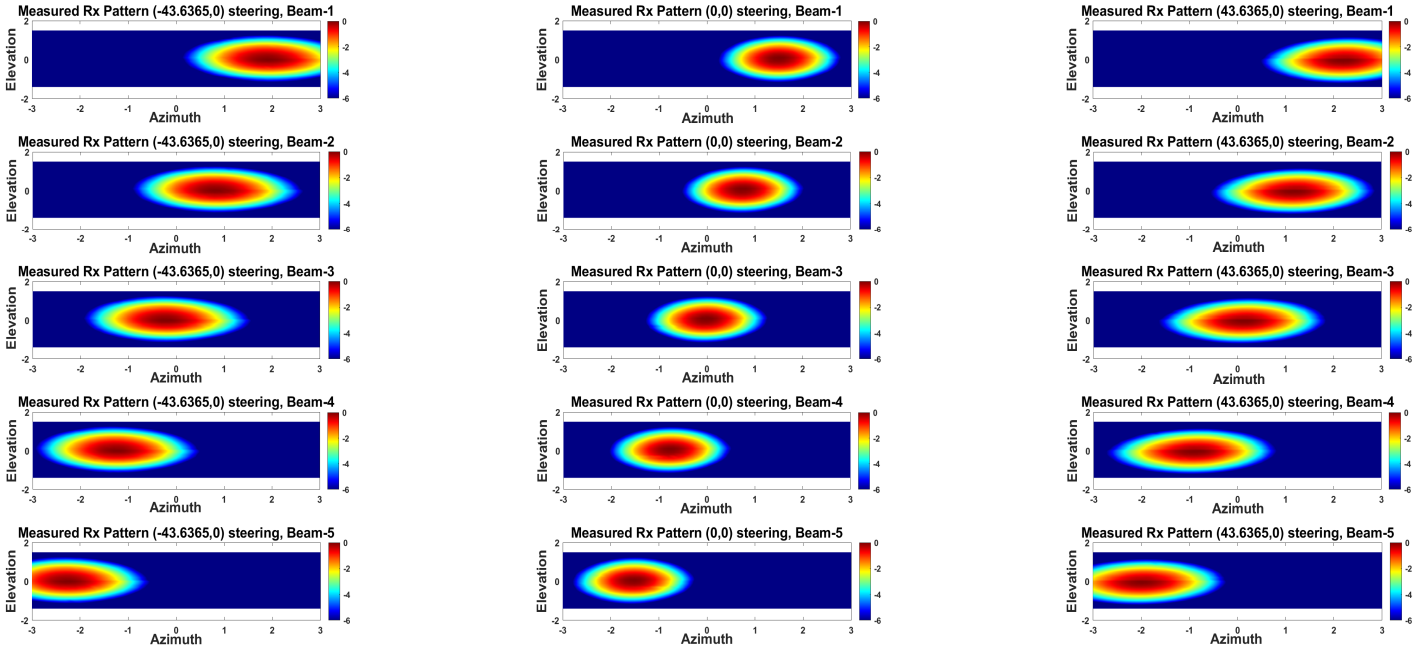

(a) Measured receive patterns.

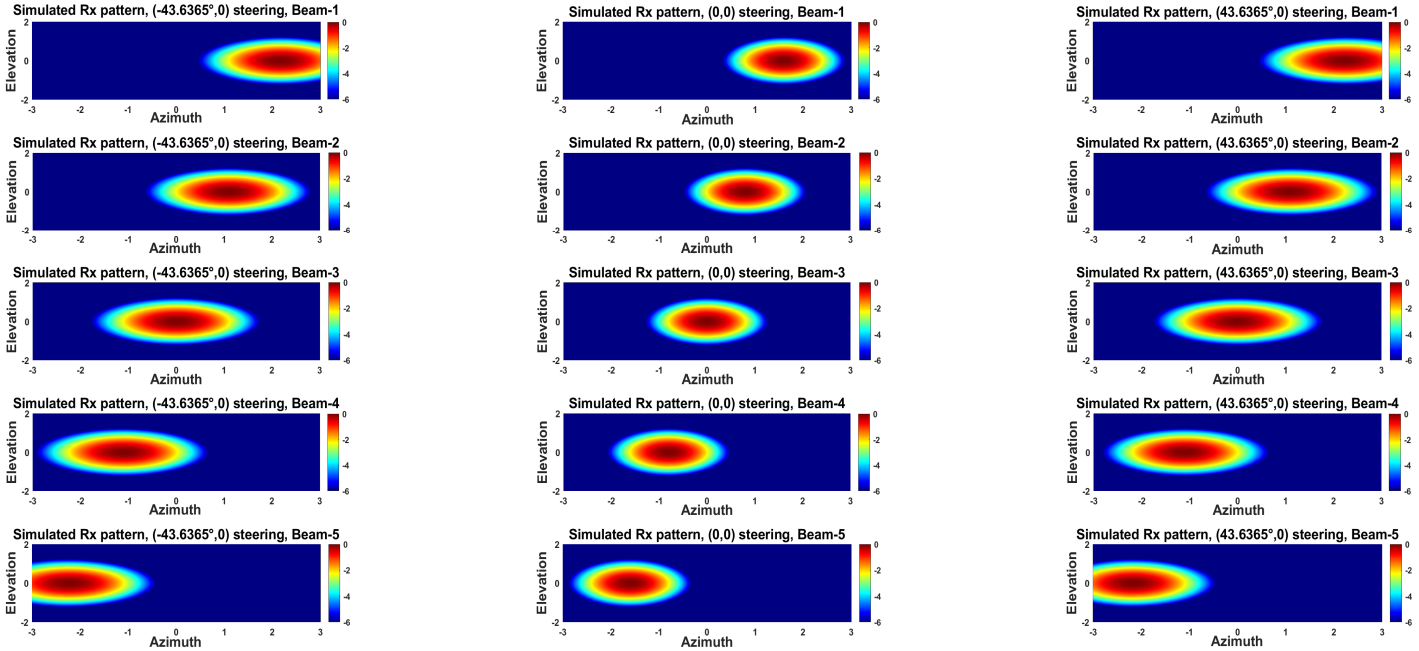

(b) Simulated receive patterns.

Figure 3.5: Comparison of receive pencil beams from spoiled beam operations for $El = 0^{\circ}$.

- The receive beam 3s are exactly the same as the receive beams in the pencil beam operations.
- The receive beam 1s,2s,4s and 5s are slightly different because they are digitally steered versions of beam 3.
- The receive beams are less smooth than the expected simulated beams.
- The distortions from the receive pencil beams and the spoiled transmit beams can combine to produce a more distorted two-way beam.

3.2 Performance metrics for two-way beams

In this section, we evaluate the performance of two-way beam patterns for spoiled beam operations by evaluating metrics discussed in Section 2.3 for the different beam patterns produced by spoiled beam operations. The weather measurements are obtained using two-way patterns. Hence, it is important to evaluate and characterize the performance of these beam patterns. As discussed in Section 2.2.2, with spoiled beam operations, a single spoiled transmit beam produces five two-way beams. Furthermore, it was observed in Section 3.1 that the measured spoiled transmit beam pattern has variations across azimuth. So, the different two-way beams with different relative azimuth positions can have non-ideal variations. For clearer comparisons, we group the two-way beams based on their relative position and label each group using the relative offset in azimuth, resulting in five beam groups. For example, all the two-way beams produced from the receive beams with an offset of $\Delta\phi = BW^p/2$ from the spoiled transmit beam (referred to as beam 2 in the previous section) are grouped together with a label $BW/2$. This way of grouping the two-way beams minimizes the effect of variation of spoiled transmit beam pattern in the azimuth and solely focuses on the effect of steering.

3.2.1 Peak power

Peak power is the maximum power in the two-way pattern. The location of the peak power in azimuth is called the peak location. The peak power, H_1, and its location ϕ_1 are illustrated for an ideal example pattern in Figure 3.6. The peak power provides a measure of the radar sensitivity. A higher peak power implies better radar sensitivity given everything else in the system is the same except changes in transmit pattern. The peak power is obtained by estimating the maximum of the power pattern in dB scale. The metric evaluated in this work is the relative peak power, which is the difference of peak power of the candidate pattern and the peak power of the corresponding broadside pattern ($\phi = 0, El = 0.9^{\circ}$). The metric is computed using this method for both the simulated and measured beam patterns. Figure 3.7 shows the variation of the relative peak power

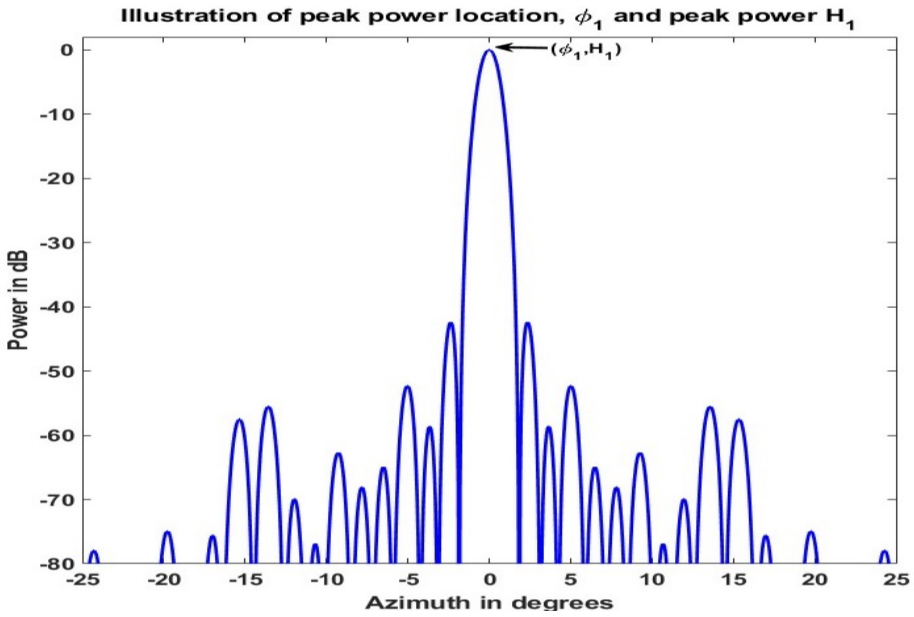

Figure 3.6: Illustration of peak-location and peak power.

of the two-way pencil beams as a function of the pencil transmit beam's electronic steering angle in the azimuth for a fixed elevation of $El = 0.9^{\circ}$. Figure 3.8 shows the variation of the relative peak power of the two-way beams, obtained from spoiled beam operations as a function of the spoiled trasnmit beam's electronic steering angle in azimuth for $El = 0.9^{\circ}$. The five subplots in Figure 3.8 show the relative peak power for the five two-way beam groups from spoiled beam

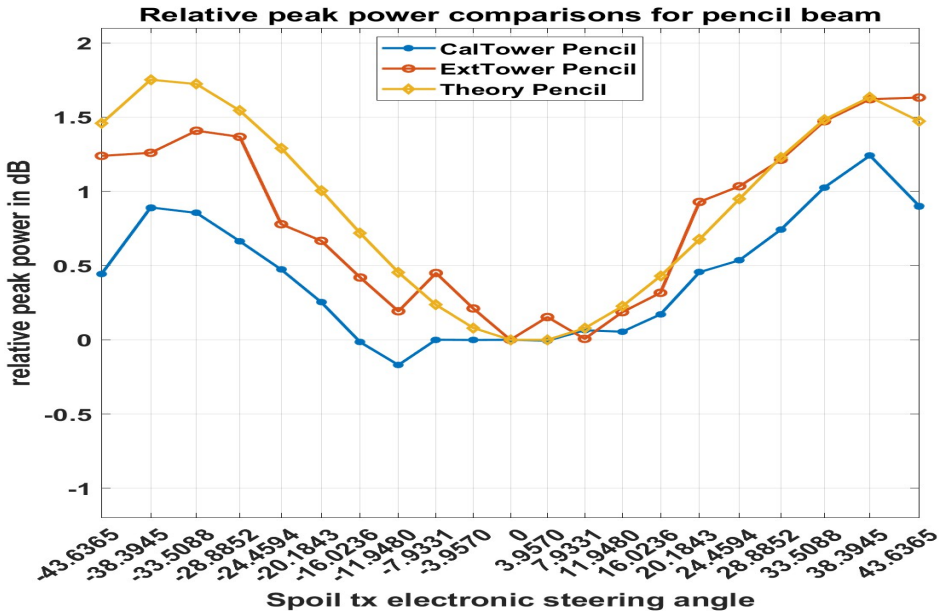

Figure 3.7: Relative peak power comparisons for pencil beam operations.

operations. The yellow curve corresponds to the variation in the relative peak power obtained from the simulated two-way beam patterns. The red curve corresponds to the metric evaluated for beam patterns obtained by external tower measurements, and the blue color curve corresponds to the metric evaluated from the beam patterns obtained from cal-tower measurements. We make the following observations from Figure 3.7 and Figure 3.8,

- The shape of the curves corresponding to the simulated results correlate with the element pattern shown in Section 3.1.1 for both pencil and spoiled beams.
- For both spoiled and pencil beams, the shape of the cal-tower plot follows the theoretical plot for the steering angles $\phi \leq -20.1843^{\circ}$ and $\phi > 28.8852^{\circ}$. For the other steering angles, the shape departs from the theoretical curve.
- For both spoiled and pencil beam operations, the shape of the external tower plot has more outliers, but it also follows the general trend of the theoretical plot.
- All the above observations hold for spoiled beams in all the beam groups.

The following inferences can be made from the above observations:

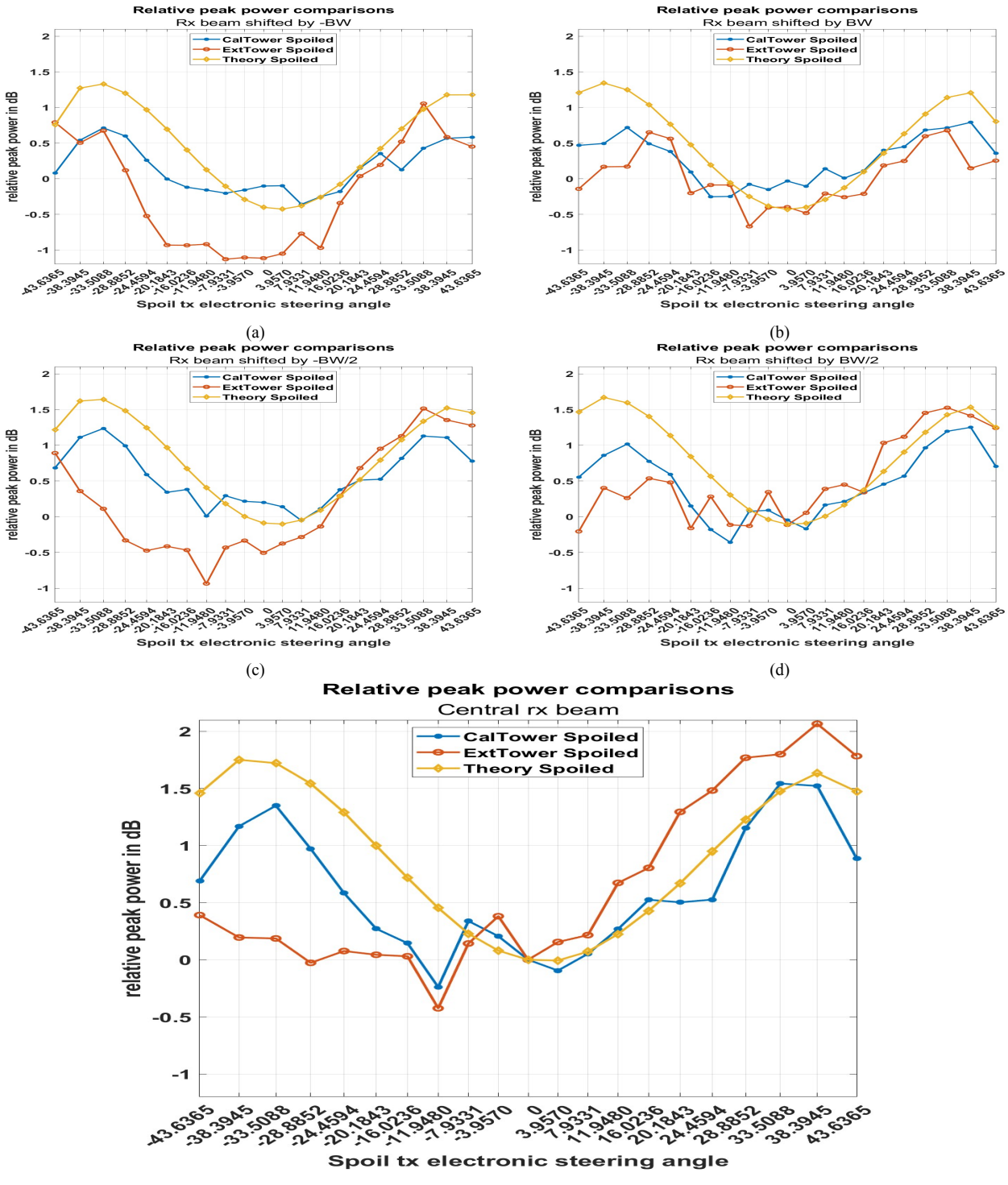

Figure 3.8: Relative peak power comparisons for spoiled beam operations. The central beam plot is expanded for more clarity.

- The peak power variation is expected to be a parabolic curve with a maximum at 0° azimuth and tapering off as we move away from broadside.
- The differences between measured and simulated metrics seems consistent between pencil and spoiled beams. Hence, we can conclude that similar distortions affect both.
- We observe that the element pattern effects are dominant, resulting in a theoretical curve that is directly correlated with the element patterns.
- The differences in the shape of the curves obtained from the theoretical patterns and the measured patterns for the beams close to broadside could also be explained by the asymmetry in the ridge locations in transmit and receive element patterns.
- A part of the reason for the differences in the values of the metric for the measured and theoretical patterns could be attributed to the measurements and environmental errors.

In order to independently study the effect of the transmit and receive patterns on the final two-way spoiled beam pattern, we evaluated the relative peak power metric for two new "pseudo-patterns" obtained by

- Meas-Tx/Sim-Rx: Combining the measured (cal-tower) transmit beam with the simulated receive beams.
- Sim-Tx/ Meas-Rx: Combining the simulated transmit beam with the measured (cal-tower) receive beams.

Figure 3.9 shows a comparison of the metric evaluated for the beams from the two pseudo-patterns, simulated patterns, and the cal-tower measurements for all the beam groups. From the figure, we observe that the blue curve obtained from cal-tower measurement patterns are more correlated with the purple curve corresponding to Meas-Tx/Sim-Rx for beam groups $-BW$, $-BW/2$ and the central beam. However, it's more correlated with the green curve corresponding to Sim-Tx/ Meas-Rx for the other beam groups. Hence, we can conclude that the distortions in both the transmit and receive patterns affect the relative peak power metric depending on the beam group.

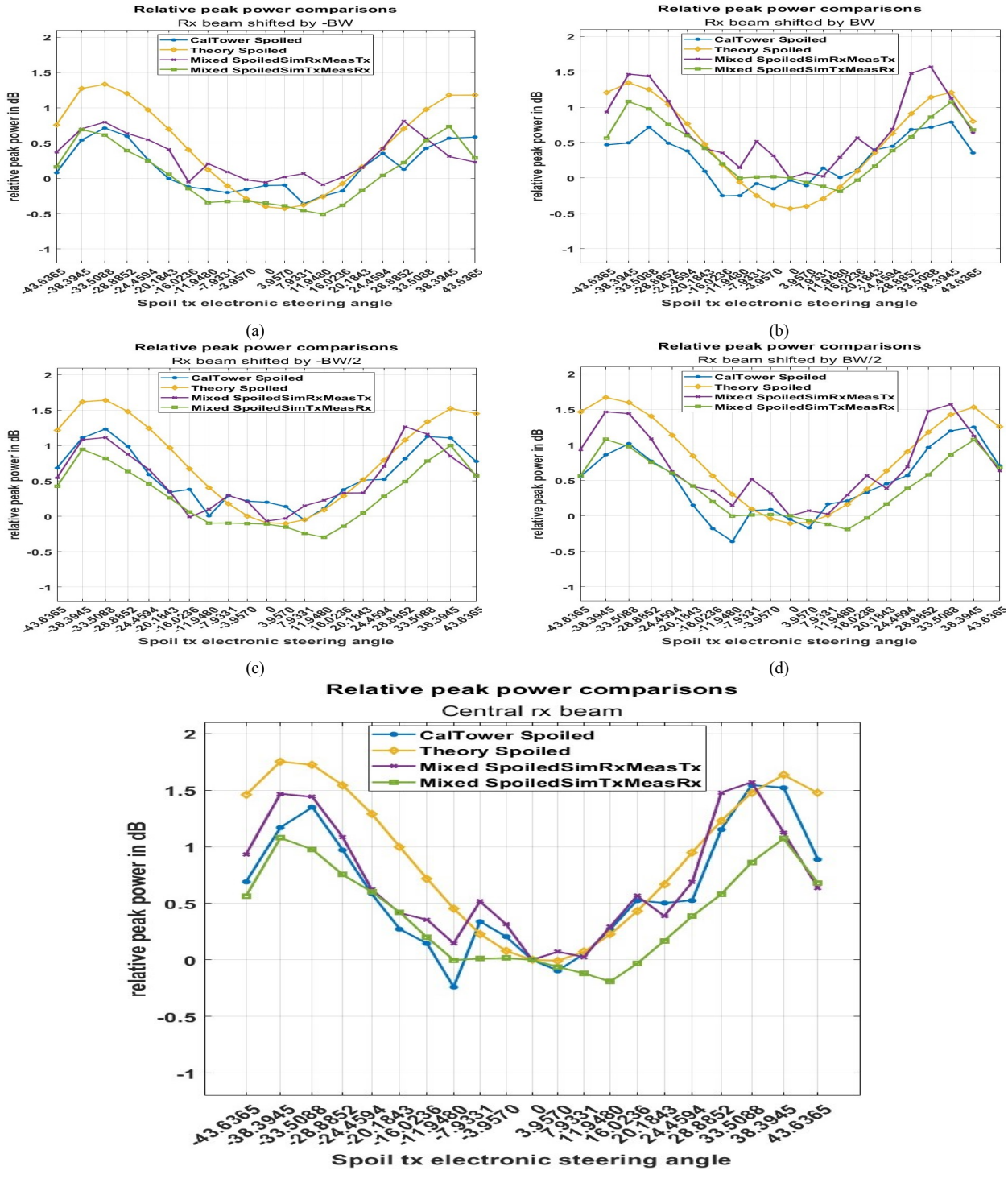

Figure 3.9: Relative peak power comparisons with "pseudo-patterns". The central beam plot is expanded for more clarity.

3.2.2 Half-power beamwidth

The angular separation between the two half-power points is the half-power beamwidth (HPBW) as illustrated in Figure 3.10. HPBW affects the angular resolution; a smaller HPBW provides a higher angular resolution. In order to estimate HPBW, we first need to estimate half-power locations as follows. Let $v(\phi)$ denote the vector with pattern power values in dB scale. Then, the half-power location estimates are given by the following steps,

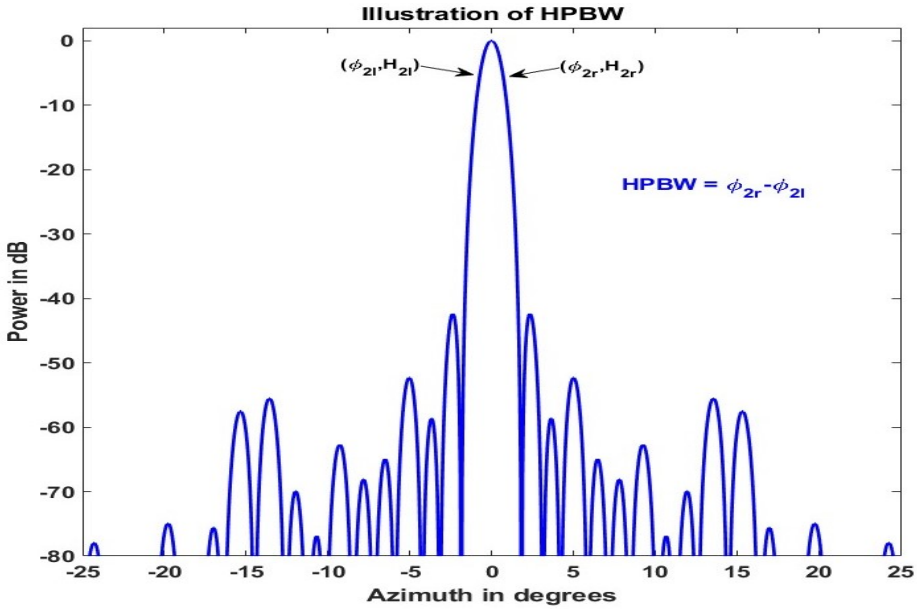

Figure 3.10: Illustration of HPBW.

1. Initial estimates: $[\overline{\phi}_{2l}, \overline{\phi}_{2r}] = \arg\min_{\phi} |v(\phi) - (H_1 - 8)|$, where H_1 is the peak power.

2. Curve fitting: Fit a 4^{th} degree polynomial to the data whose domain is $\phi = [\overline{\phi}_{2l}, \ldots, \overline{\phi}_{2r}]$ and range is $v = [v(\overline{\phi}_{2l}), \ldots, v(\overline{\phi}_{2r})]$.

3. Grid for interpolation: The interpolation grid is obtained by $\phi_I = [\overline{\phi}_{2l}, \overline{\phi}_{2l}+\delta, \overline{\phi}_{2l}+2\delta, \ldots, \overline{\phi}_{2r}]$, with $\delta = \frac{\overline{\phi}_{2r} - \overline{\phi}_{2l}}{M}$, where M is the number of samples for interpolation.

4. Estimate the interpolated power values by evaluating the value of the polynomial over the interpolation grid ϕ_I to obtain v_I.

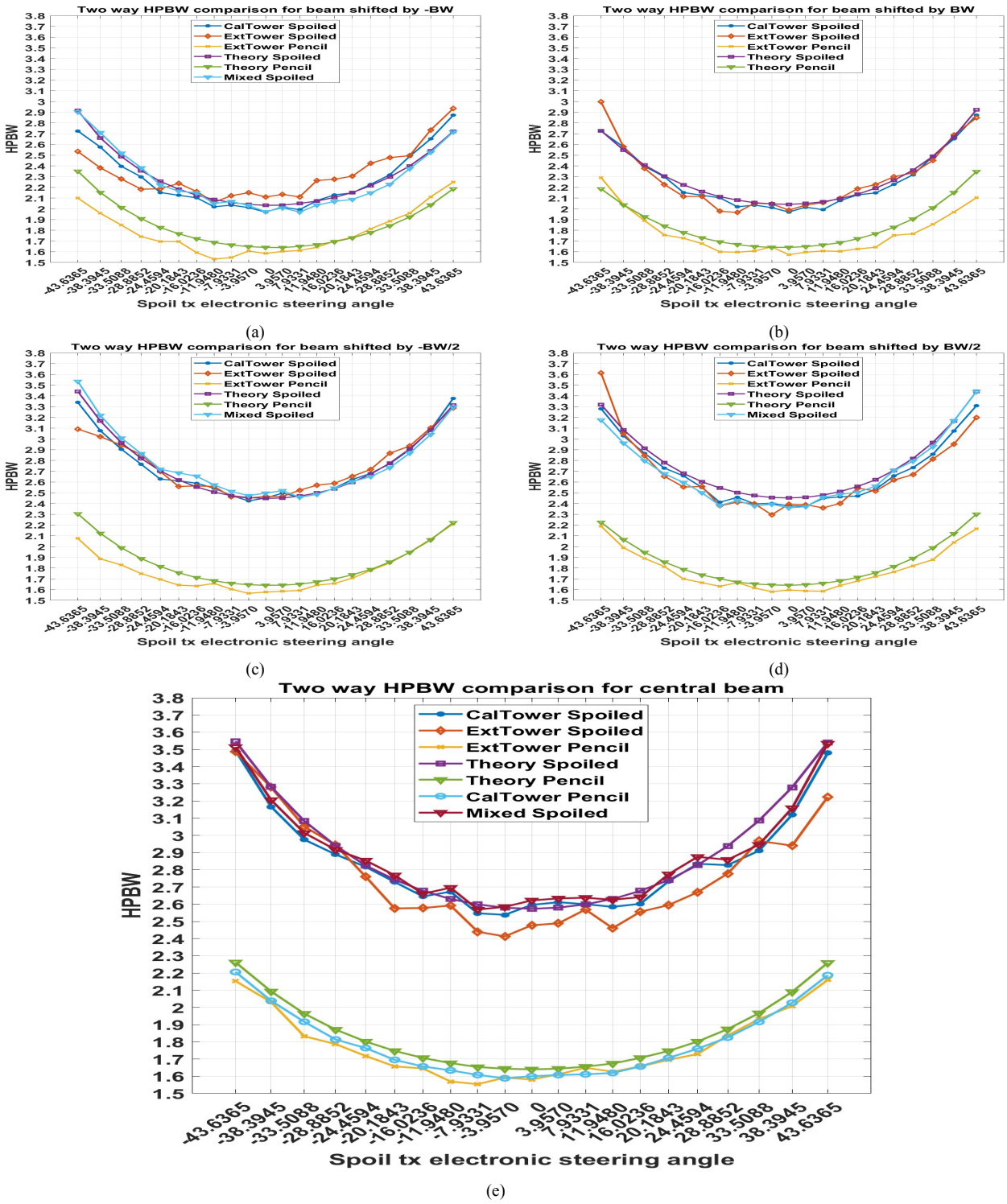

Figure 3.11: Comparison of HPBW for spoiled and pencil beam operations. The central beam plot is expanded for more clarity.

5. Final estimates: $[\hat{\phi}_{2l}, \hat{\phi}_{2r}] = \arg\min_{\phi_I} |v_I(\phi_I) - (\tilde{H}_1 - 6)|$, where $\tilde{H}_1$ is the maximum value in the vector v_I.

6. With the estimates of half-power locations as $\hat{\phi}_{2r}$ and $\hat{\phi}_{2l}$. The HPBW is given by, HPBW $= \hat{\phi}_{2r} - \hat{\phi}_{2l}$.

7. The following additional checks are made to ensure that $\hat{\phi}_{2l}$ occurs before the peak and $\hat{\phi}_{2r}$ occurs after the peak.

8. Check $\hat{\phi}_{2l} < \phi_1$, otherwise make the interpolation grid finer (set a higher value to M) and repeat steps 4 to 7.

9. Similarly, check $\hat{\phi}_{2r} > \phi_1$, otherwise make the interpolation grid finer (set a higher value to M) and repeat steps 4 to 7.

10. Check for continuity around ϕ_1 by ensuring $(v(\phi_1) - v(\phi_k)) < 2$, for ϕ_k in the neighborhood of ϕ_1.

The HPBW is computed using the above steps for the simulated and measured beam patterns that are obtained as discussed in Section 2.3.

Figure 3.11 shows the comparison of HPBW spoiled transmit beam's electronic steering angle in the azimuth for $El = 0.9^{\circ}$. The five sub-plots in Figure 3.11 show the HPBW for the five two-way beam groups from spoiled beam operations. For the cal-tower collections, the two-way pencil beam patterns are only available for the locations corresponding to the central spoiled beam group because the measurements for pencil beam operations were collected only at the transmit directions of the spoiled transmit beam. Hence, the HPBW metric is available for this scenario only for the pencil beams that correspond to the spoiled central beams. Different colors are used to highlight the source of the pattern used for evaluating the metric. These are labeled in the legend of the plots. For example, the blue curve corresponds to HPBW evaluated from spoiled-beam patterns obtained from the cal-tower. We make the following observations from Figure 3.11

- The beamwidth increases as we steer away from zero azimuth for all the beam groups.

- Furthermore, the beamwidth increase is larger for the two-way spoiled beams compared to the pencil beams.
- The HPBW obtained from cal-tower patterns follows the HPBW obtained from theoretical patterns closely for all five beam groups. The differences in the HPBW between the theory and the cal-tower measurements are always 0.2° (with a majority within 0.1°).
- The HPBW from the external tower measurements has more variation for the spoiled beam operations. The variations are less for the external tower patterns from pencil beam operations.
- The differences between measured and simulated metrics seem smaller for pencil beam operations than for spoiled beam operations. Hence, we can conclude that the performance of pencil beam operations are closer to theoretical performances. This could be caused by environmental and practical issues on the system, such as the look-up table for the phase-shifters having a bigger effect on the spoiled beams than pencil beams.

The following inferences can be made from the above observations:

- The HPBW for the spoiled beams is close to the HPBW obtained from simulations.
- The higher variations for the HPBW from the external tower patterns could be attributed to measurement and environmental errors.

3.2.3 Integrated main-lobe level

The integrated main-lobe level (IML) is defined as the area of the pattern in the region spanned between the half-power points as illustrated by the green area in Figure 3.12. In general, high IML means less power in the sidelobes. Hence, sidelobe contamination would be reduced if the ratio of IML to the integrated sidelobe level (ISL) increases. To obtain the integrated main-lobe power, the pattern is converted to the linear scale. Let the vector $\mathbf{z}(\phi)$ denote the vector with power values in linear scale. The estimate of integrated main-lobe power in linear scale is obtained as

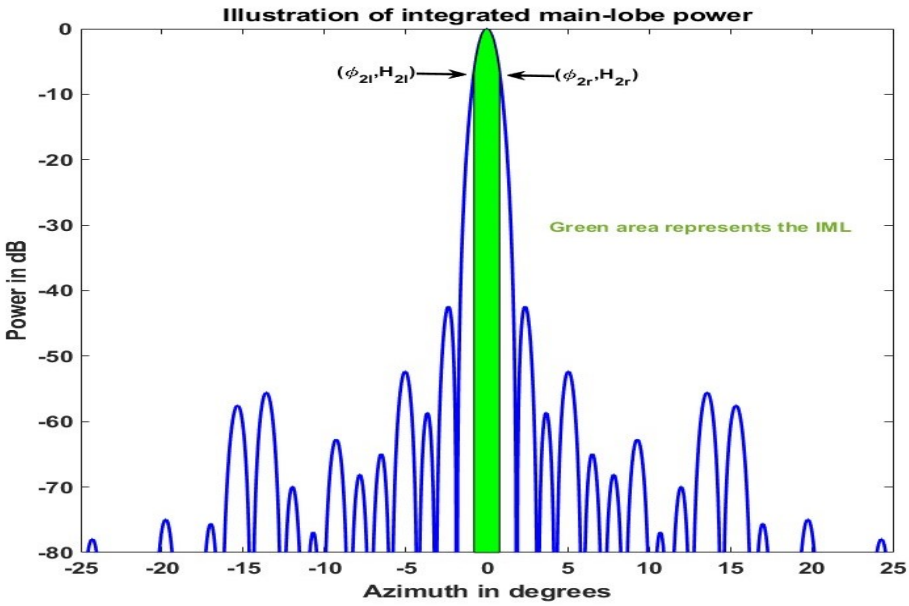

Figure 3.12: Illustration of integrated main-lobe power (IML).

$f = \sum_{i=\phi_{2l}}^{\phi_{2r}} \mathbf{z}(\phi_i)\delta\phi_i$, where $\delta\phi_i$ is the spacing of the grid ϕ_I. The IML estimate is then obtained in dB scale as $10\log_{10} f$. The metric evaluated in this work is the relative integrated main-lobe level,

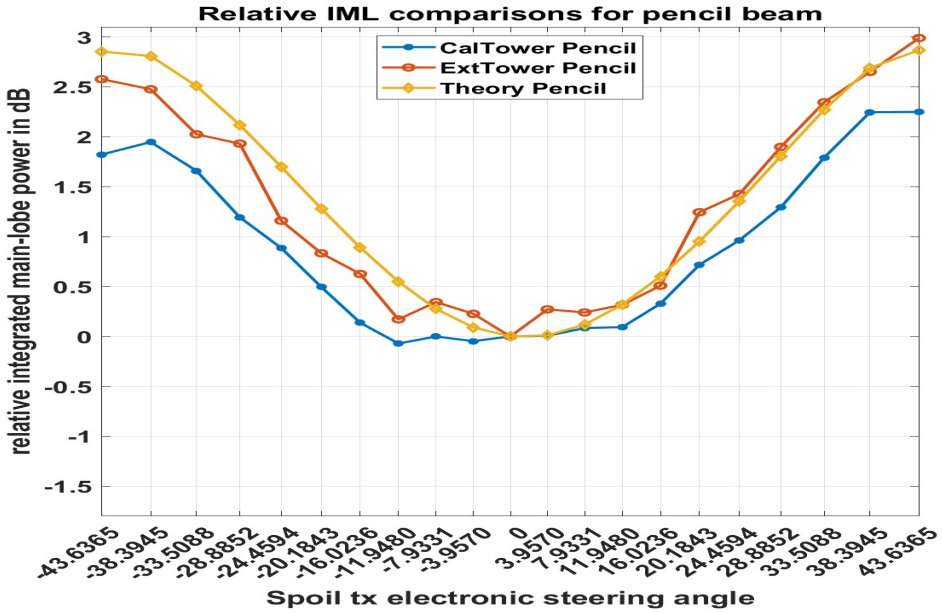

Figure 3.13: Relative IML comparisons for pencil beam operations.

which is the difference of IML of the candidate pattern and the IML of the corresponding broadside pattern. The metric is computed by the above method for the beam patterns that are obtained as

discussed in Section 2.3. Figure 3.13 shows the variation of the relative IML as a function of the

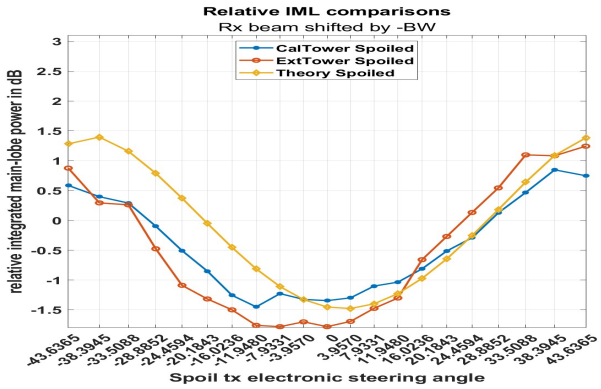

(a)

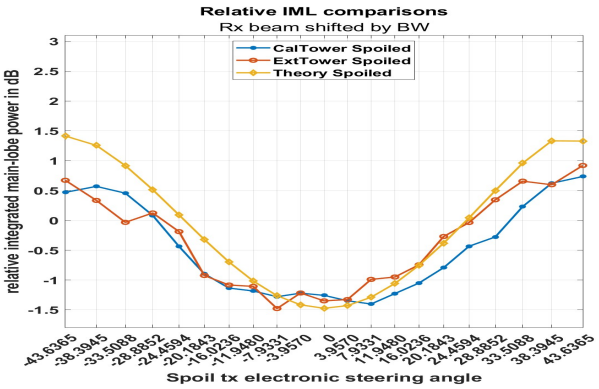

(b)

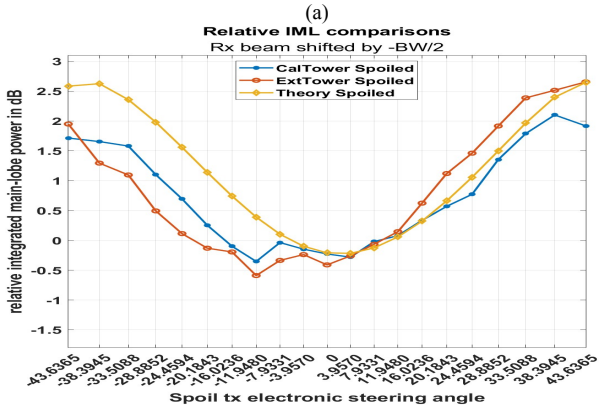

(c)

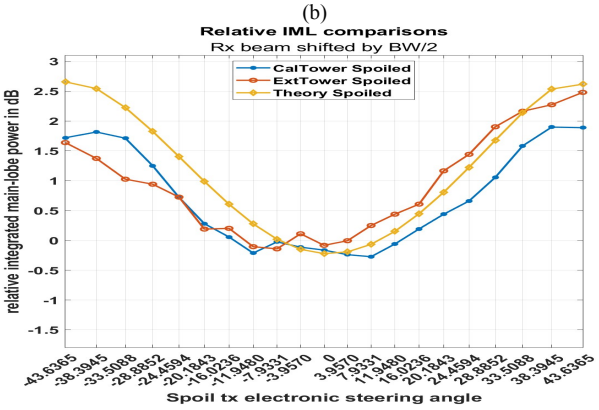

(d)

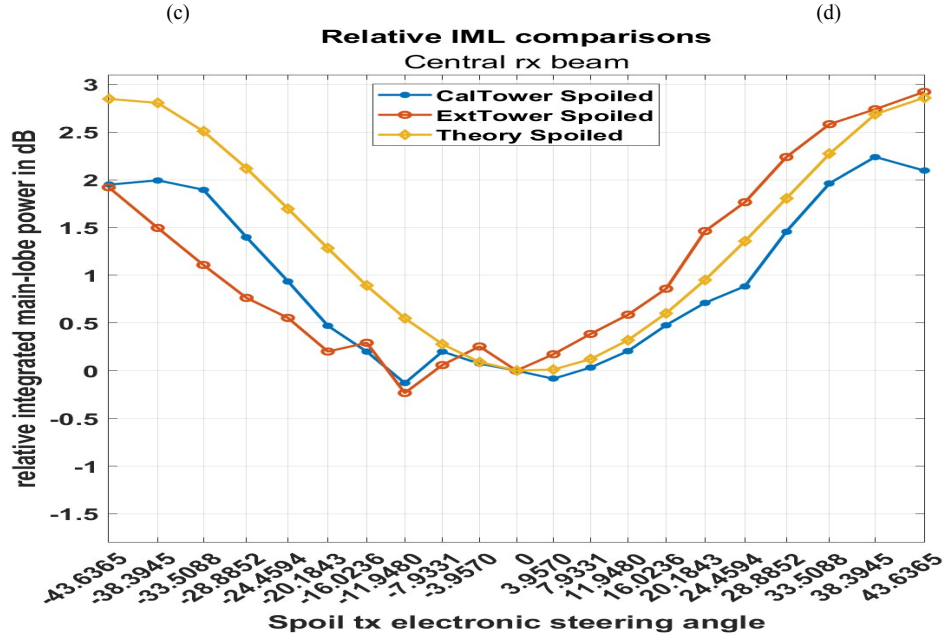

(e)

Figure 3.14: Relative IML comparisons for spoiled beam operations. The central beam plot is expanded for more clarity.

spoiled transmit steering azimuth angle for the pencil beam operations. Figure 3.14 shows the variation of relative IML as a function of the spoiled transmit steering azimuth angle for spoiled beam operations. The five sub-plots in Figure 3.14 show the relative IML variations for the five two-way beam groups from spoiled beam operations. The color scheme used for the plots here is the same as the one used in the relative peak power plots discussed above. We make the following observations from Figure 3.13 and Figure 3.14,

- The IML plot from the external tower patterns is closer to the IML plot from simulated patterns for pencil beam operations.
- The shape of the IML plot from cal tower patterns resembles the IML plot from simulated patterns in Figure 3.14.
- The shape of the IML plot from simulated patterns is correlated to the element patterns for both the operations.
- The edge beam group (beams shifted by BW, referred to as beam 5s above) have lower IML than both the beam groups shifted by $BW/2$ and the central beam group for spoiled beam operations.
- For spoiled beam operations, the shape of the cal-tower plot follows the theoretical plot for the steering angles $\phi \leq -20.1843^{\circ}$ and $\phi > 28.8852^{\circ}$. For the other steering angles, the shape is much different from the theoretical curve.
- The shape of the IML metric curves are very similar to the shape of the peak power metric plots, indicating that the same underlying phenomena may affect both metrics.

The following inferences can be made from the above observations

- The measured IML variation follows the element pattern as expected theoretically.
- From the observations, it again appears that the element pattern effects are dominant, resulting in a theoretical curve that is correlated with the element patterns.

- From the plots, it appears that the IML metric for the measured patterns flattens out for transmit angles close to 0°.
- The IML metric seems smoother (with fewer outliers) than the peak-power metric, probably because of the integration used for evaluating IML.
- The differences in the values of the metric for the measured and theoretical patterns could be partly attributed to measurement and environmental errors.
- The differences between measured and simulated metrics are consistent between pencil and spoiled beam operations. Hence, we can conclude that similar distortions affect both the operations.

3.2.4 Peak sidelobe level

The peak sidelobe level (PSL) is the maximum power of the sidelobes relative to the peak-power as illustrated in Figure 3.15. The peak sidelobe level gives a measure of the maximum contamination that is possible from the pattern and the environment, relative to the peak power. In order to evaluate the PSL, we first need to estimate the first-null points. First null points are the first points beyond the peak where power is at a local minimum in a well-behaved pattern. We first estimate the first null points in the pattern by checking the changes in the slope beyond the peak along both directions. The points ϕ_{3l} and ϕ_{3r} in Figure 3.15 represent the first null points. Let $\mathbf{v}_l(\phi)$ and $\mathbf{v}_r(\phi)$ denote the vectors of pattern powers in dB, in the region $\phi < \phi_{3l}$ and $\phi > \phi_{3r}$ respectively. Then, the peak sidelobe power is given by,

$$S_p = \max_{v}([v_l(\phi), v_r(\phi)] - H_1) \tag{3.1}$$

The metric evaluated in this work is the relative peak sidelobe power, that is the difference of PSL power of the candidate pattern and the PSL power of the corresponding broadside pattern. PSL is computed by the above method for the simulated and cal-tower beam patterns and are obtained as discussed in Section 2.3.

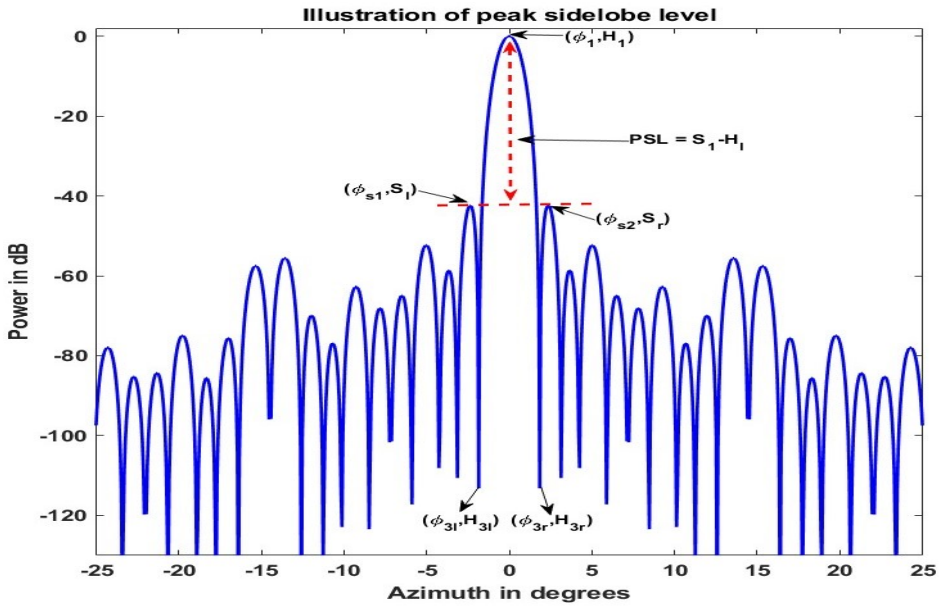

Figure 3.15: Illustration of peak sidelobe level.

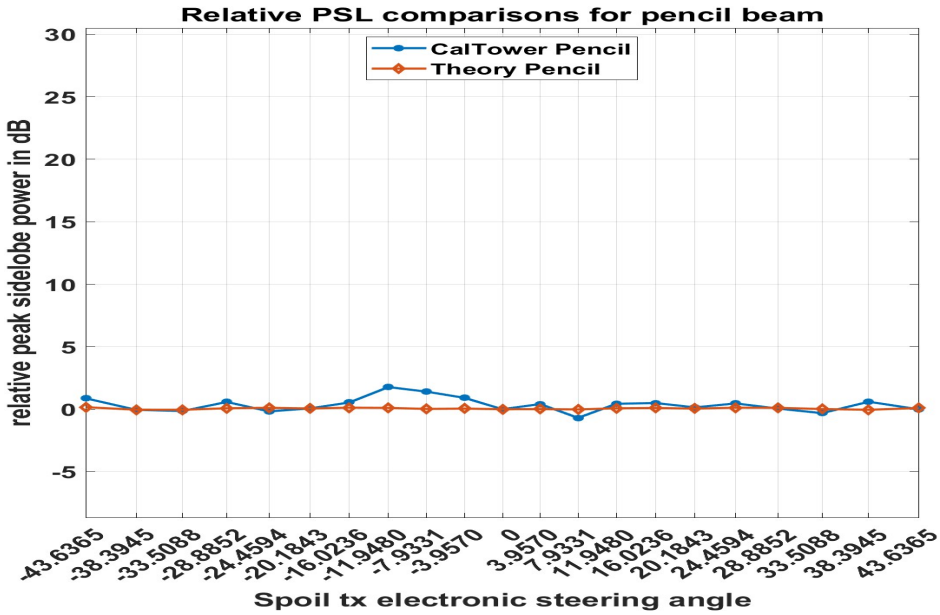

Figure 3.16: Relative PSL comparisons for pencil beam operations.

Figures 3.16 and 3.17 show the variation of the relative PSL with different spoiled beam transmit locations for the pencil and spoiled beam operations respectively. The five sub-plots in Figure 3.17 show the relative PSL variations for the five two-way beam groups from spoiled beam operations. The red-color curves correspond to the relative PSL evaluated from simulated patterns. The blue color curves correspond to the relative PSL evaluated from cal-tower patterns. We make

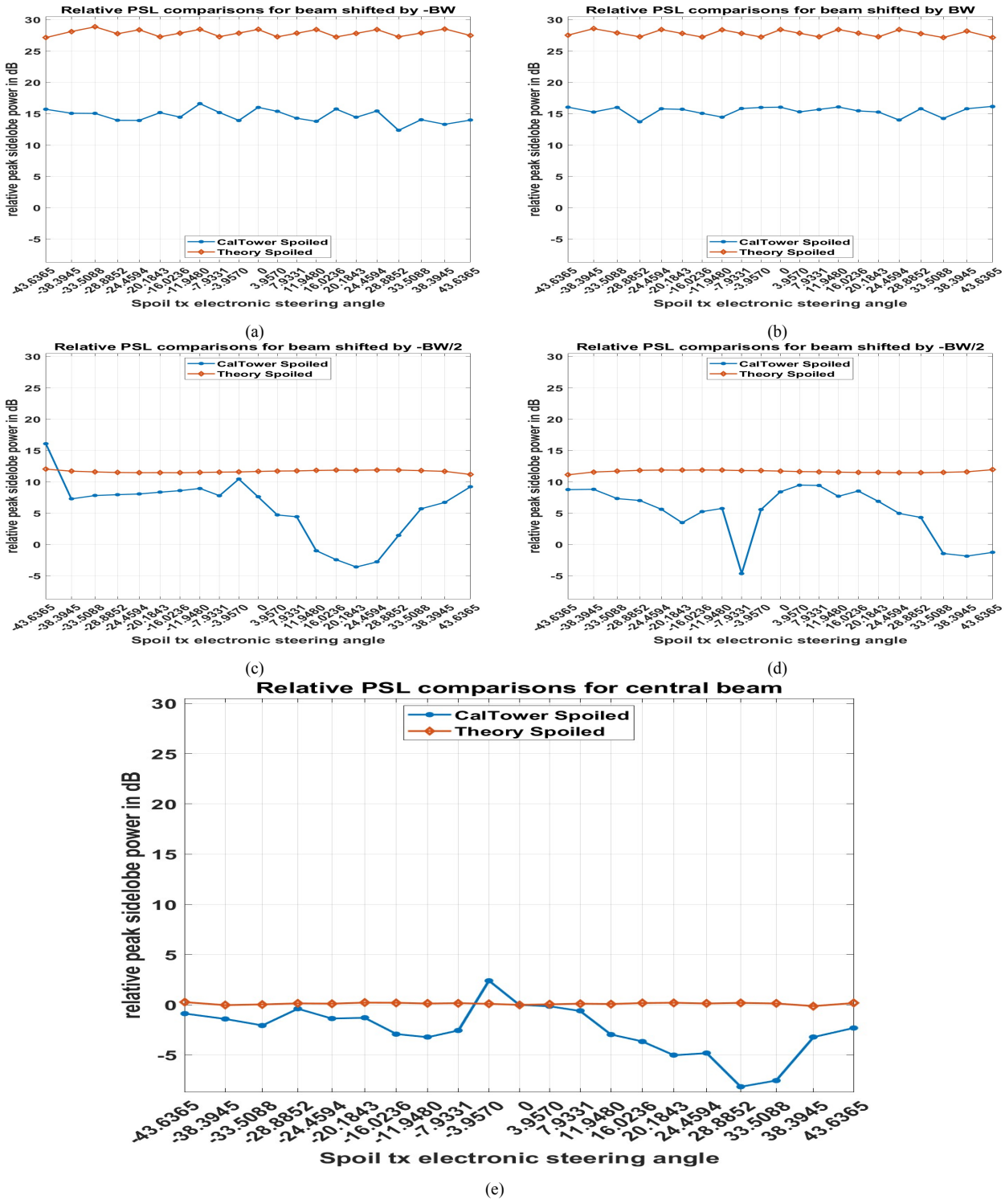

Figure 3.17: Relative PSL comparisons for spoiled beam operations. The central beam plot is expanded for more clarity.

the following observations from Figures 3.16 and 3.17,

- The PSL from the measured cal-tower patterns matches well with the PSL from the simulated patterns for pencil beam operations.
- For the spoiled beam operations, the edge beams have much higher PSL compared to the central beam.
- The PSL curve from simulated patterns is very close to a constant for the pencil beam,the central beam group (beam 3s), and the $\pm BW/2$ beam groups (beam 2s and beam 4s). It resembles a noisy line for the $\pm BW$ beam groups (beam 1s and beam 5s).
- The PSL curves for the measured spoiled beam patterns are very noisy with a lot of outliers.
- The differences between measured and simulated metrics seem much smaller for the pencil beam operations than for spoiled beam operations. Hence, we can conclude that the PSL estimates are more robust for the pencil beam operations.

The following inferences can be made from the above observations:

- The ideal relative-PSL pattern is expected to be flat across all the transmit directions.
- The relative-PSL curve for the pencil beam patterns is close to zero. The relative-PSL curves from theoretical spoiled beam patterns are flat but have higher relative PSLs.
- The higher relative PSL for the spoiled beam pattern for the non-central beams may be explained because the sidelobes of the receive pencil beam combine with the transmit main lobe in an asymmetric manner to raise the PSL.
- The large variation in the PSL from the measurement pattern seems to be a characteristic of the patterns.

In order to independently study the effect of the transmit and receive patterns on the final two-way spoiled beam pattern, we evaluated the relative-PSL metric for the "pseudo-patterns", Meas-Tx/Sim-Rx and Sim-Tx/Meas-Rx defined previously in Section 3.2.1.

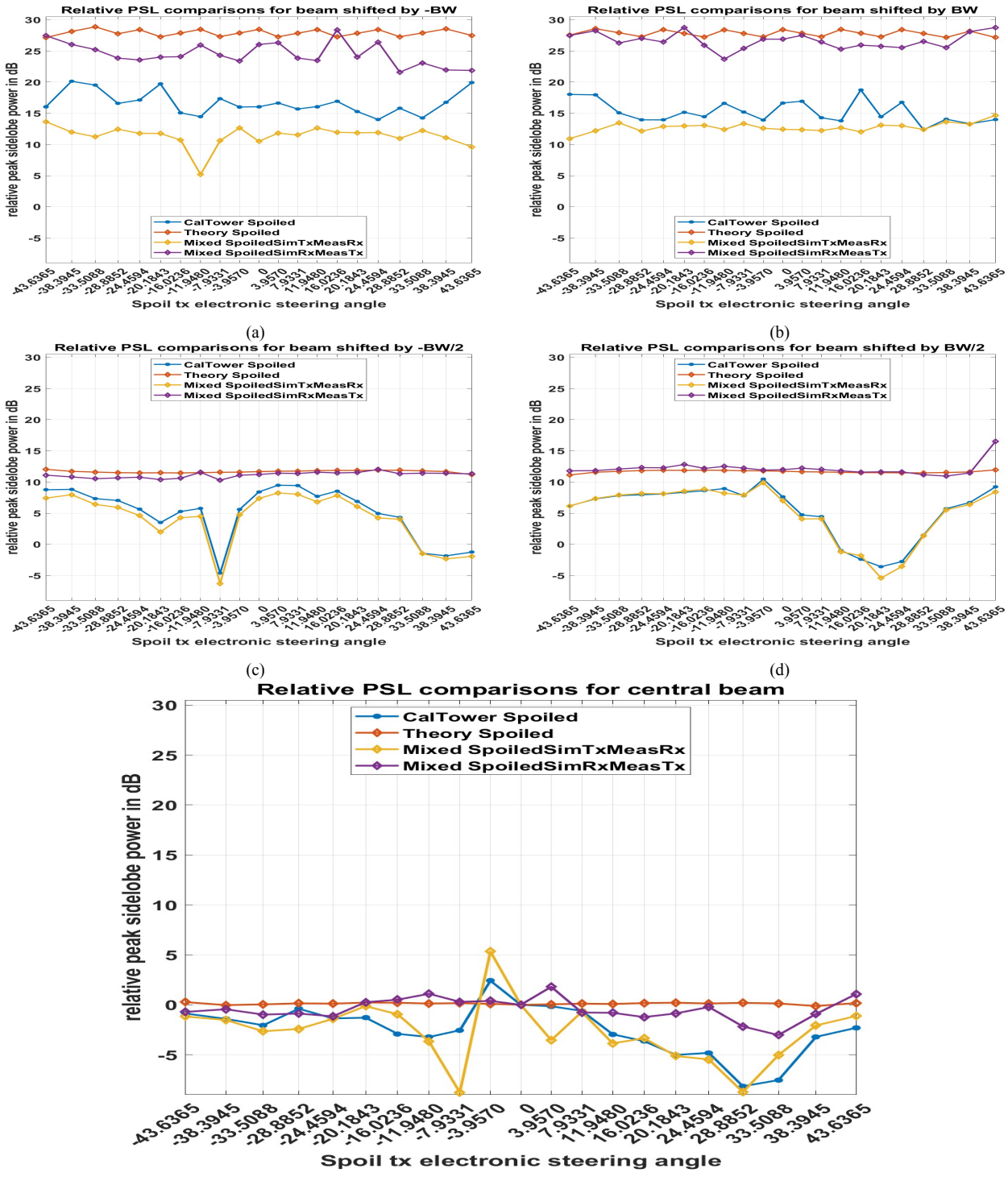

Figure 3.18: Relative PSL comparisons with "pseudo-patterns". The central beam plot is expanded for more clarity.

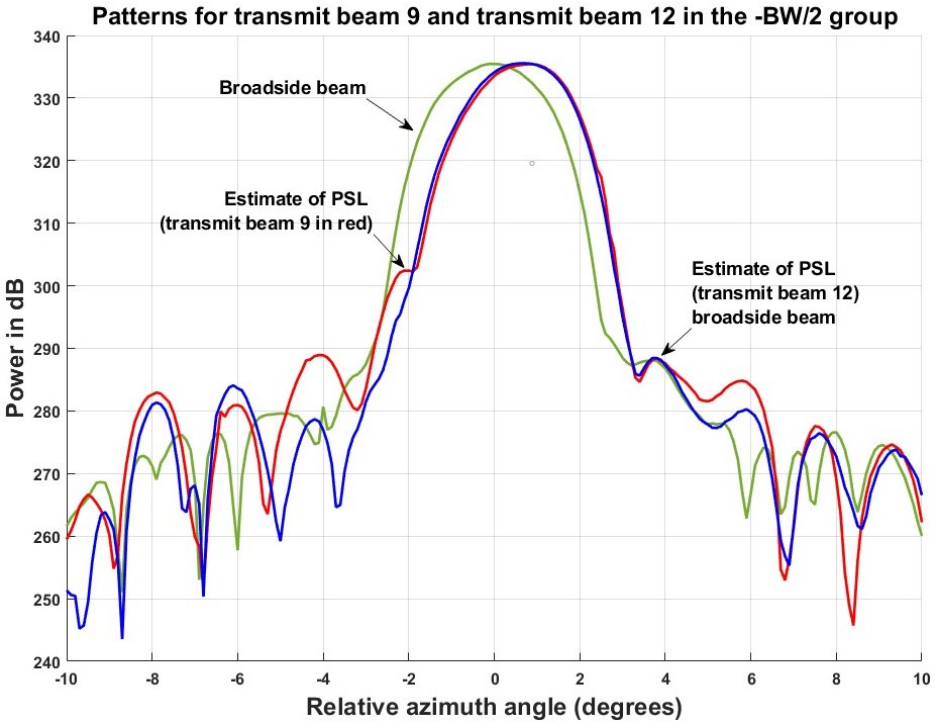

Figure 3.19: Two-way beam-patterns highlighting the PSL variations.

Figure 3.18 shows a comparison of the metric evaluated for the beams from the two pseudo-patterns, simulated patterns and the cal-tower measurements for all the beam groups. From the figure, we observe that the blue curve obtained from cal-tower measurement patterns is more correlated with the yellow curve corresponding to Sim-Tx/ Meas-Rx for all the beam groups, whereas the purple curve corresponding to Meas-Tx/Sim-Rx is more correlated to the theoretical red curve. Hence, we can conclude that the distortions in the receive beam patterns contribute to the large variations in the PSL. In order to further understand the cause of the PSL variations, we plotted the two-way beam patterns of transmit beam 9 and transmit beam 12, corresponding to the the beams with the maximum and minimum PSL variations for beam group $-BW/2$ (beam 2s) in the left plot in Figure 3.19. Similarly, the two-way beam patterns of transmit beam 10 and transmit beam 16 are plotted in the right plot. The figure shows that the "shoulders" in the two-way beam patterns raise the PSL estimates and hence reduce the relative PSL, resulting in the large minima seen in Figure 3.17 for these beam groups. In order to understand the cause of the "shoulders" in the two-way patterns, we plotted the simulated transmit, three simulated receive patterns, and the two-way

beam patterns belonging to different beam groups in Figure 3.20. From the figure, we observe that the peak sidelobe for the central beam (beam 3) is caused by the overlap of the first sidelobe of the receive beam with the area around the first null of the spoiled transmit beam (roll-off area), captured by the dashed purple arrow. The peak sidelobe for the $-BW/2$ beam (beam 2) is caused by the overlap of the first sidelobe of the receive beam with the area around the right falling edge of the spoiled transmit beam. The peak sidelobe for the $-BW$ beam (beam 1) is caused by the overlap of the main-lobe of the receive beam with the area around the left falling edge of the spoiled transmit beam. Hence, in this case the central beam has the lowest PSL followed by the $-BW/2$ beam and the $-BW$ has "shoulders", resulting in a high PSL value.

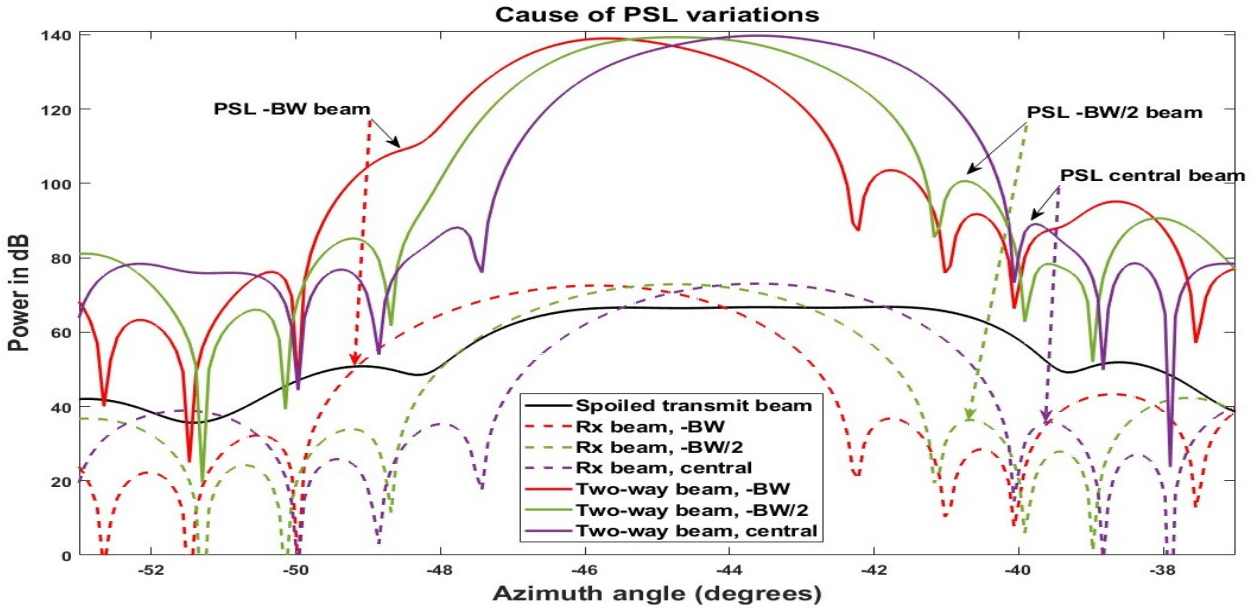

Figure 3.20: Simulated patterns to illustrate the cause of PSL variations.

3.2.5 Integrated sidelobe level

The integrated sidelobe level is the total area of the beam-pattern beyond the first nulls as illustrated in Figure 3.21. The integrated sidelobe level gives a measure of the total contamination that is possible from the environment. Let the estimates of first null points be ϕ_{3l} and ϕ_{3r}. Let the vector $\mathbf{z}(\phi)$ denote the vector with power values in linear scale. The ISL estimate in linear scale is given

by,

$$S_{ISL} = \sum_{i=1}^{\phi_{3l}-1} \mathbf{z}(\phi_i)\delta\phi_i + \sum_{i=\phi_{3r}+1}^{M} \mathbf{z}(\phi_i)\delta\phi_i \tag{3.2}$$

The ISL estimate then is converted to dB scale by $10\log_{10} S_{ISL}$. The metric evaluated in this

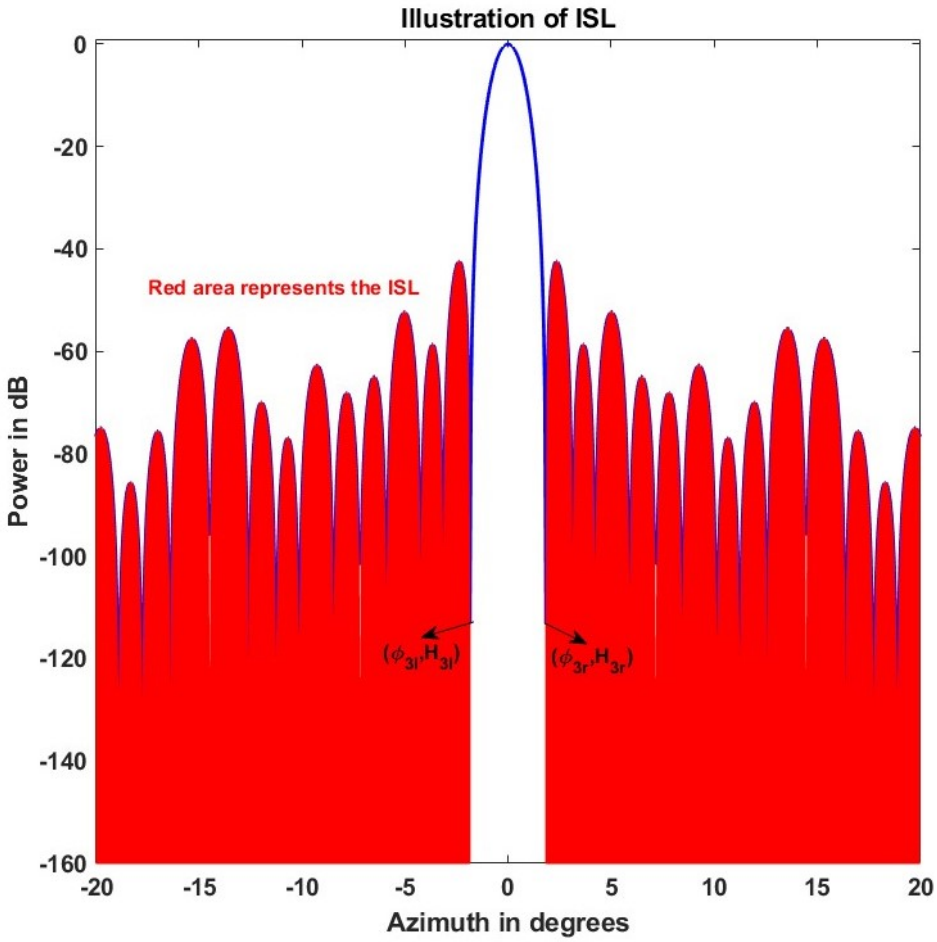

Figure 3.21: Illustration of the integrated sidelobe level.

work is the relative integrated sidelobe power, which is the difference of ISL of the candidate pattern and the ISL of the corresponding broadside pattern. Relative ISL is computed by the above method for the simulated and cal-tower beam patterns, that are obtained as discussed in Section 2.3. Figures 3.22 and 3.23 show the variation of the relative ISL with different spoiled beam transmit locations for the pencil and spoiled beam operations respectively. The five sub-plots in Figure 3.23 show the relative ISL variations for the five two-way beam groups from spoiled beam operations. The color scheme used is the same as used for PSL plots.

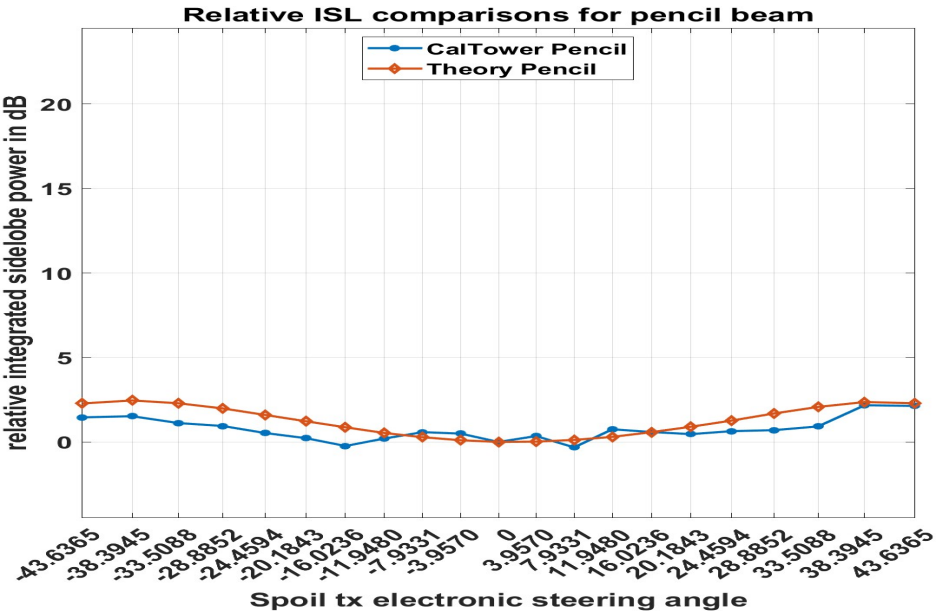

Figure 3.22: Comparison of relative ISL for pencil beam operations.

From the figures, we observe that the relative ISL plots have the same shapes as the relative PSL plots discussed above. However, the relative ISL plots are a little higher than the PSL plots because of the integration over additional sidelobes. Hence, we can make the following inferences:

- The relative ISL plot is also expected to be a straight line.
- As the ISL plots seem to be highly correlated to the PSL plots, which shows that PSL is the dominant component of ISL. For example, in Figure 3.19, the estimates of PSL for the plots in the second panel are about -33.2 dB and -47.2 dB respectively, a difference of 15 dB. The PSL points also form a part of the ISL estimate. Hence, we observe the correlation in the ISL and PSL plots.

In this chapter, we have studied the performance of the different beam patterns used for spoiled beam operations. We concluded that the ATD element patterns cause many of the variations in the main-lobe metrics such as peak power and the IML. We also concluded that the sidelobe metrics are affected mainly by the distortions in the receive beams. Some of the effects of these variations on the weather collections will be discussed in the next chapter.

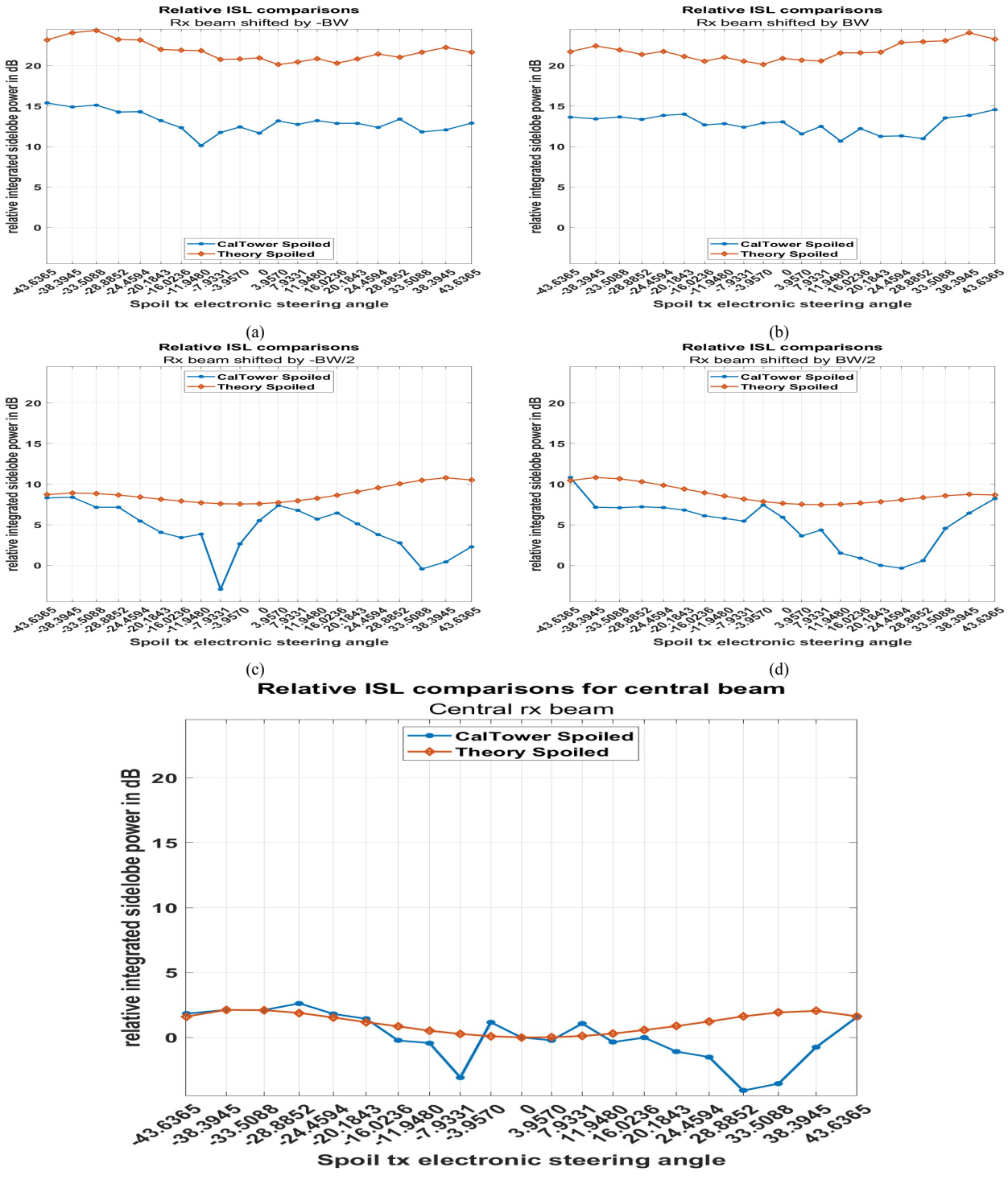

Figure 3.23: Comparison of relative ISL for spoiled beam operations. The central beam plot is expanded for more clarity.

Chapter 4

Conclusions and Future Work

In this chapter, we discuss conclusions and take-aways based on the initial performance evaluation of the spoiled beam operations. Furthermore, we also outline a plan for future work.

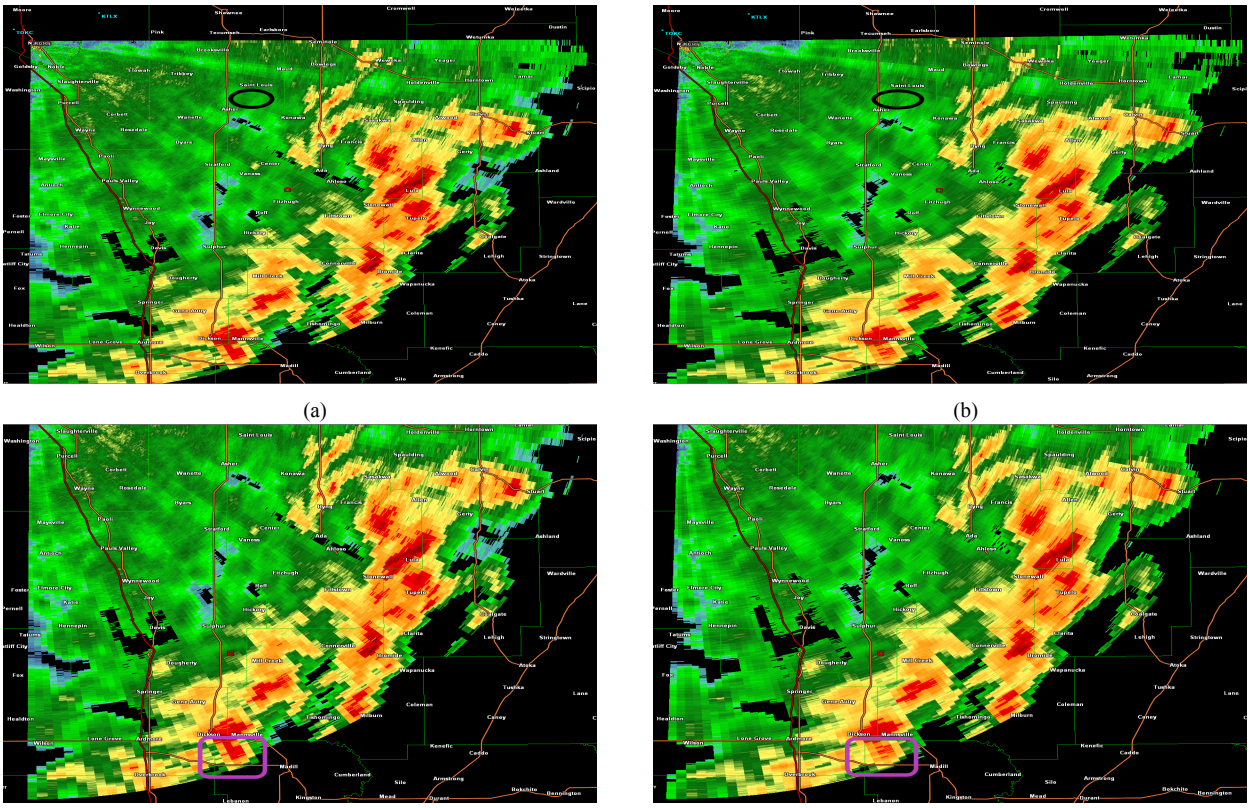

(a) (b)

(c) (d)

Figure 4.1: Comparison of weather operations with pencil beam (left column) and spoiled beam (right column) collections. ATD collection performed on 11/03/2024 at 2319 UTC.

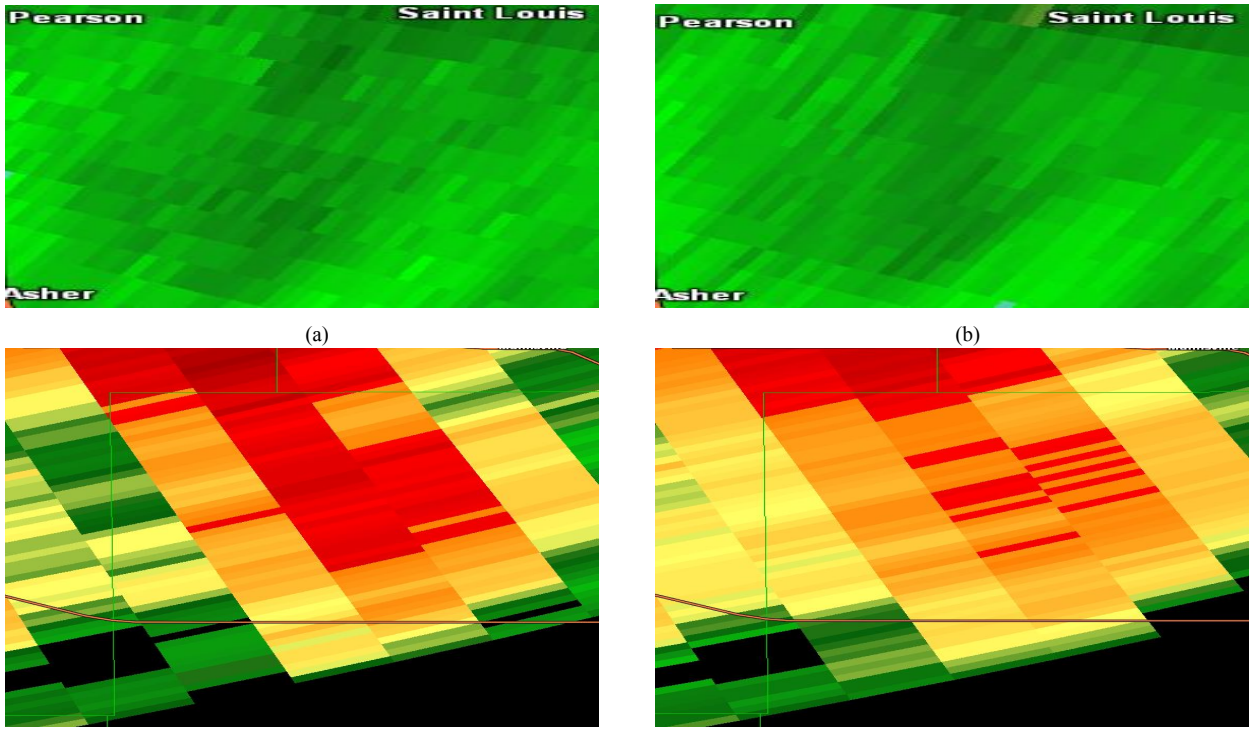

Figure 4.2: Comparison of weather operations with pencil beam (left column) and spoiled beam (right column) collections, Zoomed. Figures (a) and (b) are the zoomed areas in the dark black circle og Figure 4.1. Figures (c) and (d) are the zoomed areas in the dark pink circle of Figure 4.1.

The first set of conclusions relates to the performance of spoiled beam operations. From Section 3.1, we first concluded that the spoiled transmit beams do indeed have a wider beamwidth in azimuth that is close to the expected width and they also have the same beamwidth as the pencil beams in elevation. Next, we also concluded that the analog transmit/receive and digital receive beam-steering mechanisms are working accurately. Finally, the receive beams and the two-way beams in spoiled beam operations have pencil-beam shapes as expected.

The second set of conclusions relates to the performance of the beam patterns used in spoiled beam operations, which we evaluated through a set of metrics. We first focused on the main-lobe region of the pattern. From Section 3.1, we concluded that the elevation cuts of the transmit beam are not completely flat, which was not expected. There is a ridge of up to -1 dB at the beam center. Next, from Section 3.2, we concluded that the transmit and receive element patterns affect the peak power and the IML metrics, resulting in variations that are different from the conventional

cosine shape. Also, the distortions in the transmit patterns predominantly cause variations in the peak power and the IML metrics for the central, $-BW/2$, and $-BW$ beam groups. Similarly, the distortions in the receive patterns predominantly cause variations in the peak power and the IML metrics for the $BW/2$ and BW beam groups. Hence, main-lobe metrics are affected by distortions in the element patterns, transmit patterns, and receive patterns. We also obtained the following conclusions based on the performance of the sidelobe region of the pattern. For a fixed beam group, the theoretical PSL and ISL metrics are approximately constant over different transmit steering angles. However, among different beam groups, the theoretical PSL and ISL metrics have a large variation. For example, the relative PSL is 0 dB, 12 dB and 27.5 dB for the central, $BW/2$ and BW beam groups respectively. Hence, the sidelobe metrics have high variations over different beam groups. The variation of the sidelobe metrics from the measured patterns includes many outliers and some deviation from the theoretical metrics. Distortions in the receive beams affect the sidelobe metrics, causing the difference between values obtained from the measured and theoretical patterns. The variations of the metrics among different beam groups is due to the "shoulders" in the two-way beam patterns, which occur due to the differences in the overlapping of the spoiled transmit beam and the receive pencil beams belonging to different groups as described in Section 3.2.4. The main takeaway from these conclusions is that computing metrics from measured patterns can provide a quick way to assess performance; however, care must be taken to develop metrics that are robust to measurement artifacts or to develop artifact-free measurement techniques.

For a more practical analysis of the performance of spoiled beam operations for weather data collected, an example comparison of data collected with spoiled beams and pencil beams is provided in Figure 4.1. The figure shows reflectivity measurements from the ATD. The measurements were collected with a PPI scan, observing the sector from 90° ("earth relative") to 180° ("earth relative") with broadside at 135° ("earth relative") using pencil beam operations followed by spoiled beam operations using a spoil factor of $m = 3$ and $n = 5$ simultaneous receive beams (3×5 mode). In the figure, we observe discontinuities across adjacent radials in spoiled beam collections in the right column. A good example for comparison between pencil and spoiled beam opera-

tions is marked by a dark black circle in Figures 4.1a and 4.1b. The zoomed area around the dark black circle is shown in Figures 4.2a and 4.2b. Discontinuities in spoiled beam collections could be attributed to inaccurate calibration of spoiled beams and/or to different beam overlapping characteristics between adjacent beam groups as shown in Figure 4.3. The left panel in Figure 4.3 compares the two way beams produced from two adjacent spoiled transmit beams. These two two-way beams constitute adjacent azimuth radials in the weather operations. We observe that the "shoulders" of the two-way beam from group BW are on the right side whereas the "shoulders" of the two way beam from group $-BW$ are on the left side. For comparison, in the right panel, we show the overlap characteristics of two adjacent beams produced by a single transmit beam. Here, the two-way beam from group $-BW/2$ does not have shoulders. Hence, this difference in the overlap characteristics could be a contributor to discontinuities in the data collected with spoiled beams. Additional work on calibration of spoiled beams is needed to better explain (and address) this important aspect of the spoiled beam data. Addressing this problem should allow for a more routine use of spoiled transmit beams on the ATD, enabling significantly faster updates while preserving the coverage and quality of the data. Another observation in Figure 4.1 is the expected loss

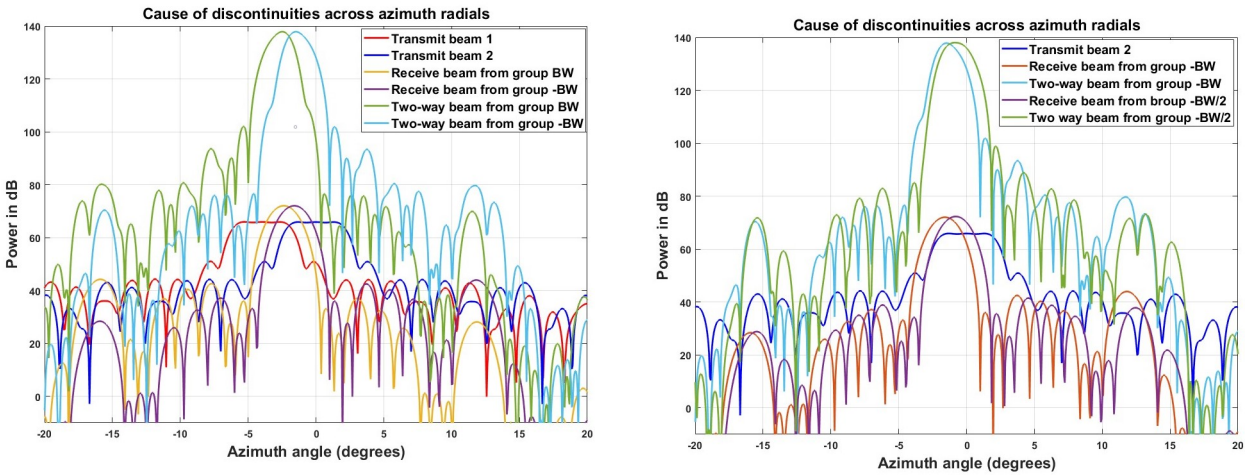

(a) (b)

Figure 4.3: Cause of discontinuities across the azimuth radials.

of angular resolution in the spoiled beam collections resulting in spatially smeared weather data. A good example of such smearing is marked by a dark pink circle in the second row of Figure 4.1.

The zoomed area around the dark pink circle is shown in Figures 4.2c and 4.2d. The variation in HPBW and large sidelobe variations over different beam groups discussed in Section 3.2 are likely causes for the weather echoes from different directions ”merging”, resulting in data with reduced spatial resolution. Finally, we also notice that, as expected, the spoiled beams in general have lower sensitivity compared to pencil beams. This reduces the storms footprints in Figures 4.1b and 4.1d.

Moving forward, we will use the metrics obtained from the measured patterns to inform the development of more accurate spoiled beam calibrations. The IML metric is promising for developing the reflectivity corrections. These could be used to compute the reflectivity corrections for a set of beams over one elevation cut. We plan to preliminarily verify this by applying the corrections derived from the IML and comparing with reflectivity obtained using conventional pencil beams. Then, we will repeat the process to obtain the corrections for higher elevations. If the reflectivity corrections are successful, we will similarly develop corrections for differential reflectivity by making systematic pattern measurements using the cal-tower with vertical polarization (V-pol) data. Furthermore, the current measurement results are for 0.9° elevation. Hence, measurements at higher elevations will be needed to complete the spoiled beam calibration. Because the spoiled beam performance is strongly dependent on the beam groups, it may be feasible to develop beam-group-dependent calibration corrections for spoiled beam operations in future.

In closing, through this initial evaluation of spoiled beam operations on the ATD, we developed important measurement tools and processes, and gained valuable insights into the current performance of this capability. To use data collected with spoiled transmit beams in support of meteorological research objectives documented in NSSL’s PAR R&D plan, additional calibration work is needed.

Appendix A

Metrics for degree-space sampling

In this appendix, we present results from evaluating the metrics discussed in Section 2.3 for two-way spoiled beam patterns produced with degree-space sampling. In general, the shape of the metrics obtained from theoretical patterns is the same for both degree-space and sine-space sampling. However, the metrics produced from the measurements have more distortions for the degree-space sampling. This is likely due to pointing inaccuracies in degree-space sampling.

A.1 Peak power

The relative peak power metric for spoiled beam and pencil beam operations are shown in Figures A.1 and A.2

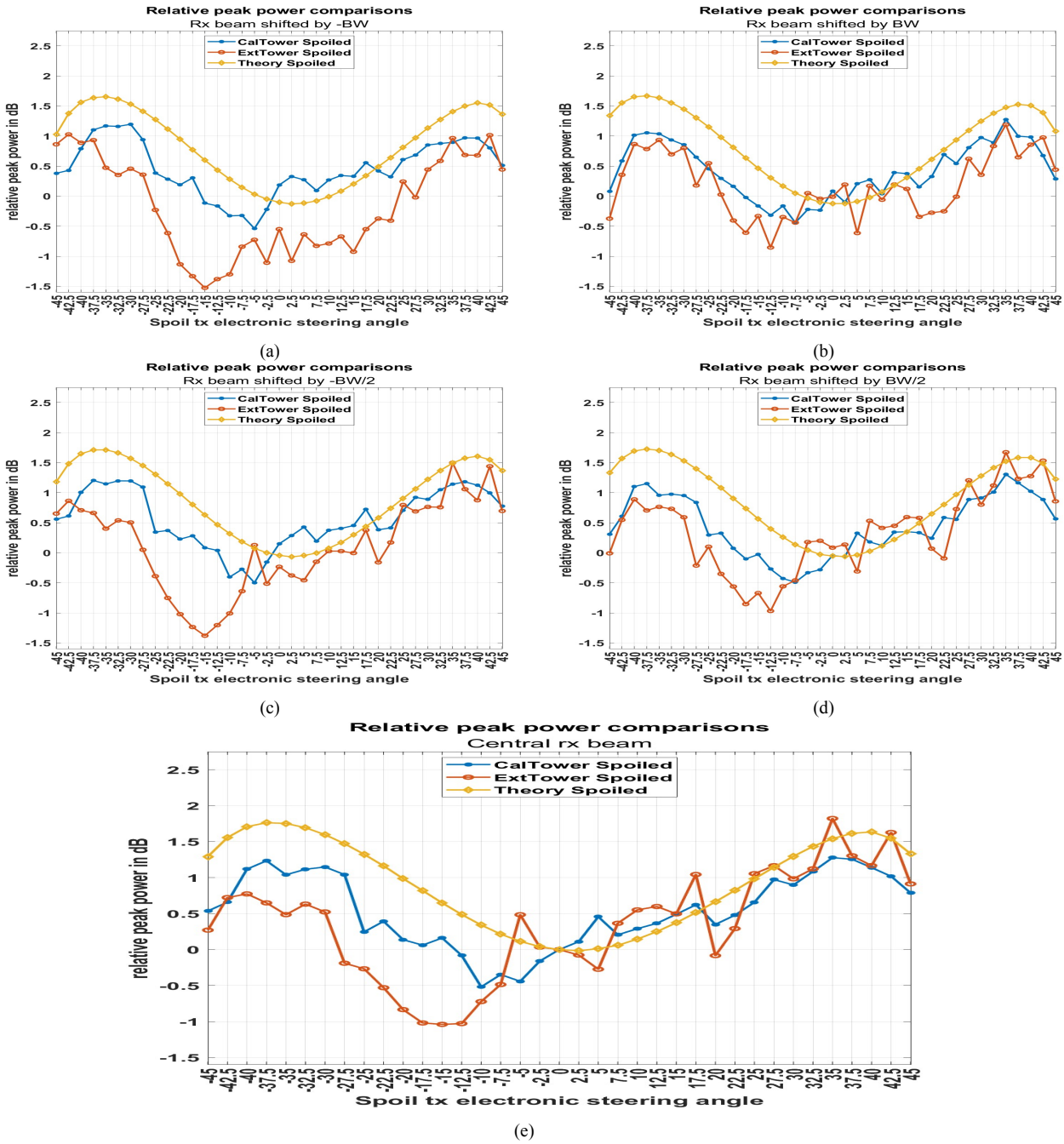

Figure A.1: Relative peak power comparisons for spoiled beam operations.

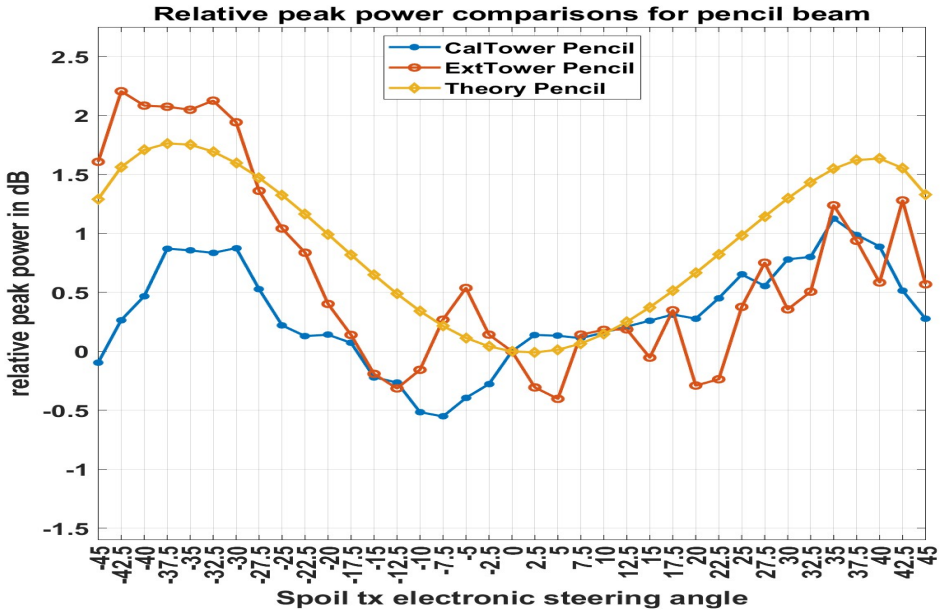

Figure A.2: Relative peak power comparisons for pencil beam operations.

A.2 IML

The relative IML metric for pencil beam and spoiled beam operations are shown in Figures A.3 and A.4

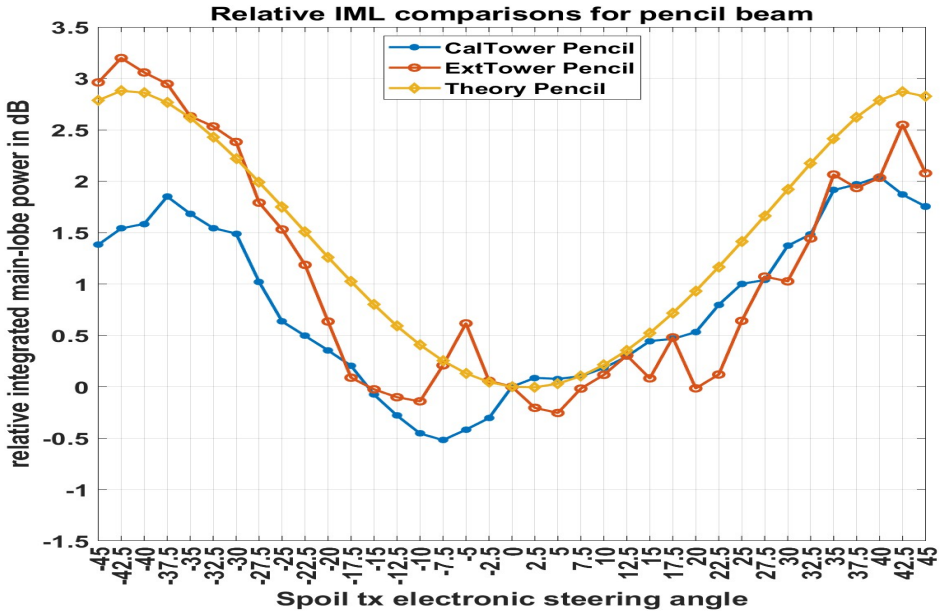

Figure A.3: Relative IML comparison for pencil beam operations.

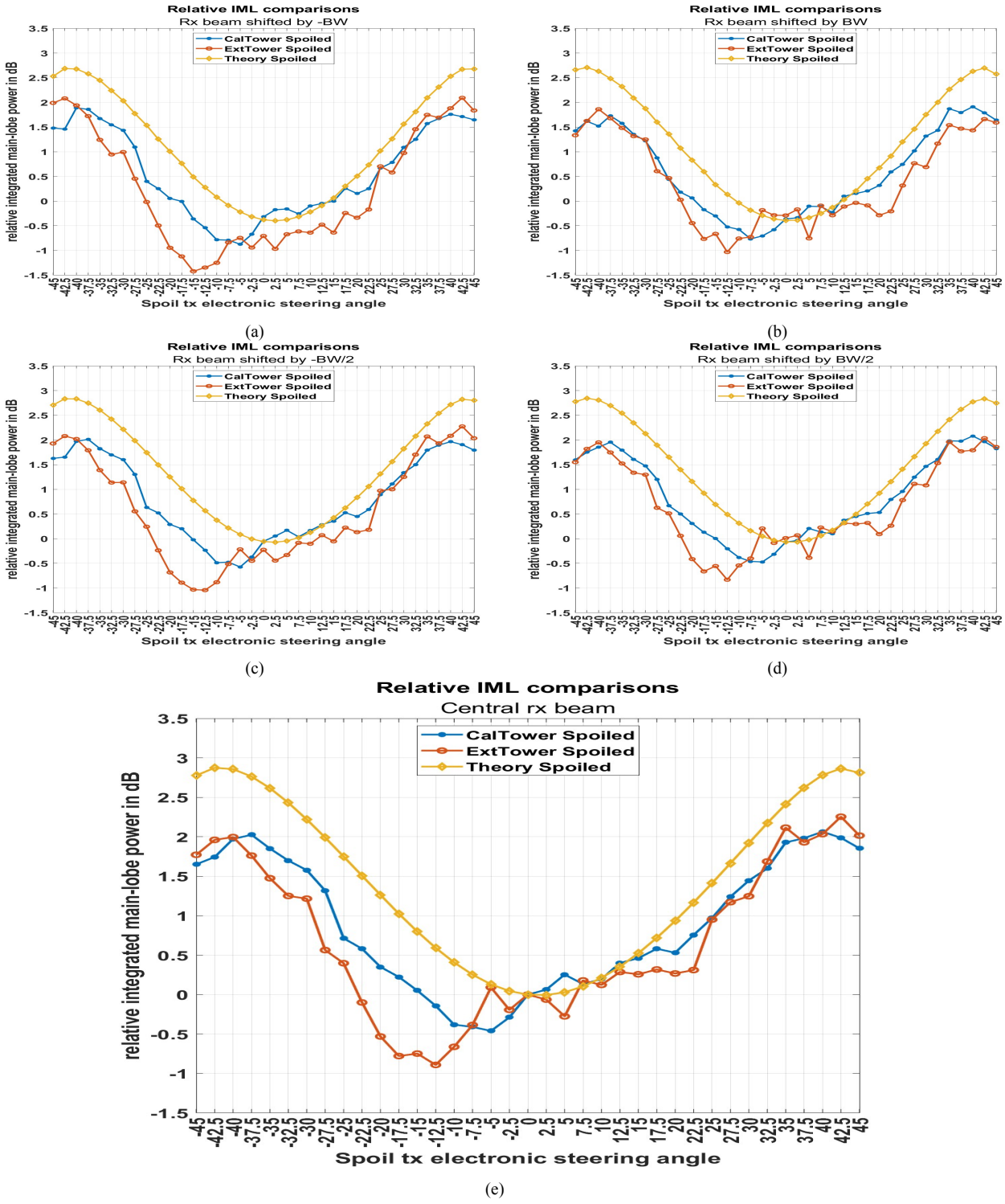

Figure A.4: Relative IML for spoiled beam operations. The central beam plot is expanded for more clarity.

A.3 PSL

The relative PSL metric for pencil beam and spoiled beam operations are shown in Figures A.6 and A.5

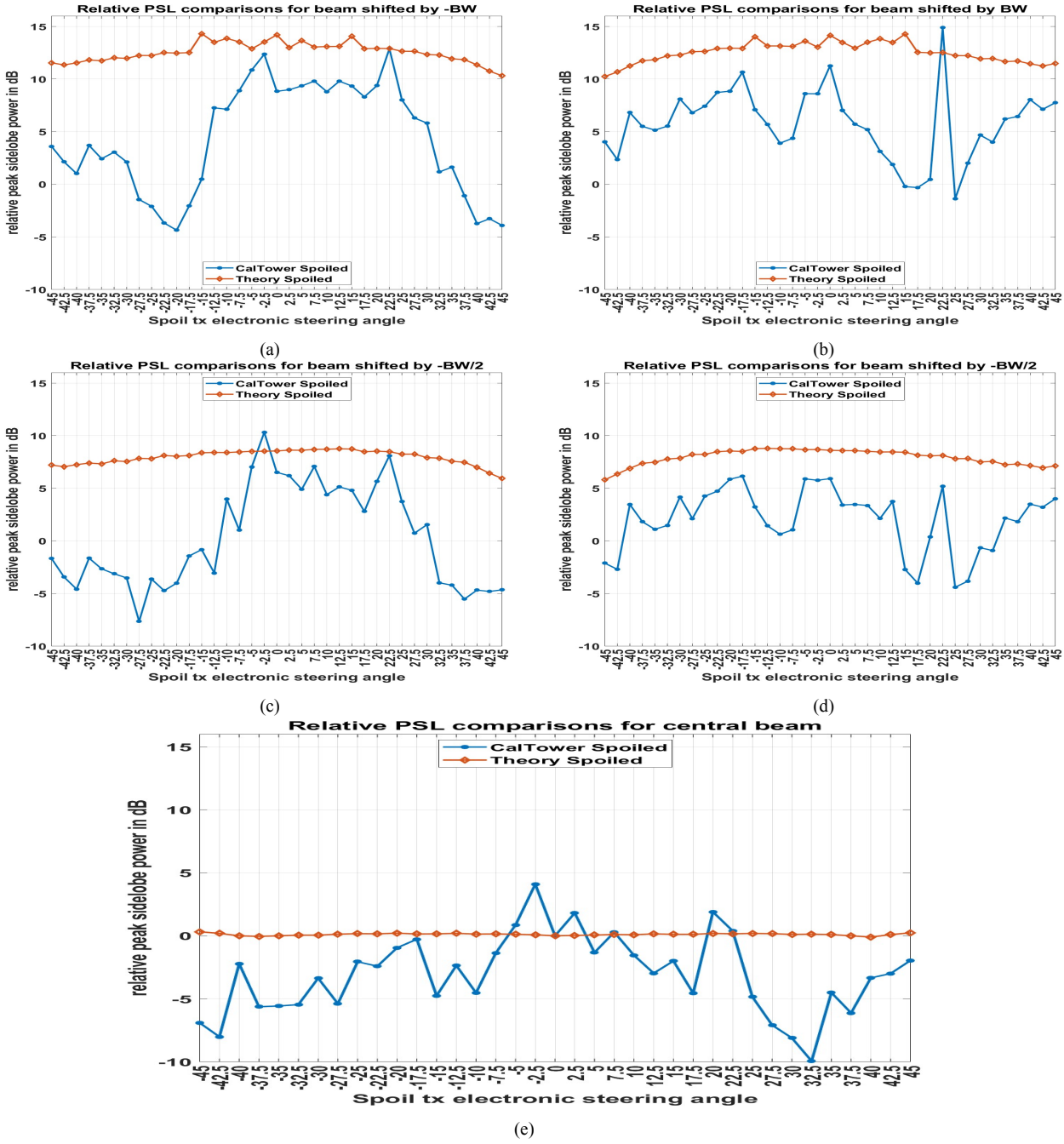

Figure A.5: Relative PSL comparisons for spoiled beam operations. The central beam plot is expanded for more clarity.

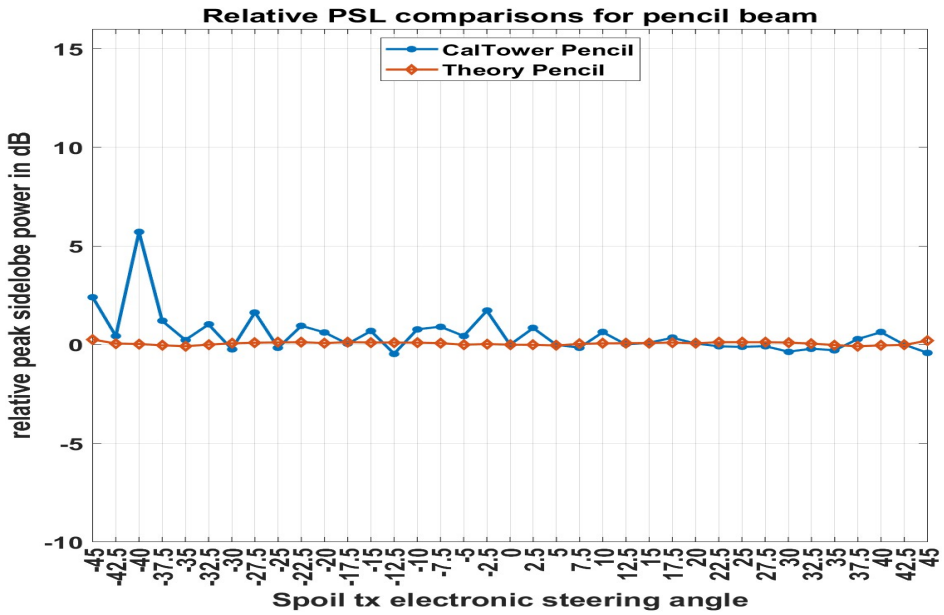

Figure A.6: Relative PSL comparison for pencil beam operations.

A.4 ISL

The relative ISL metric for pencil beam and spoiled beam operations are shown in Figures A.7 and A.8

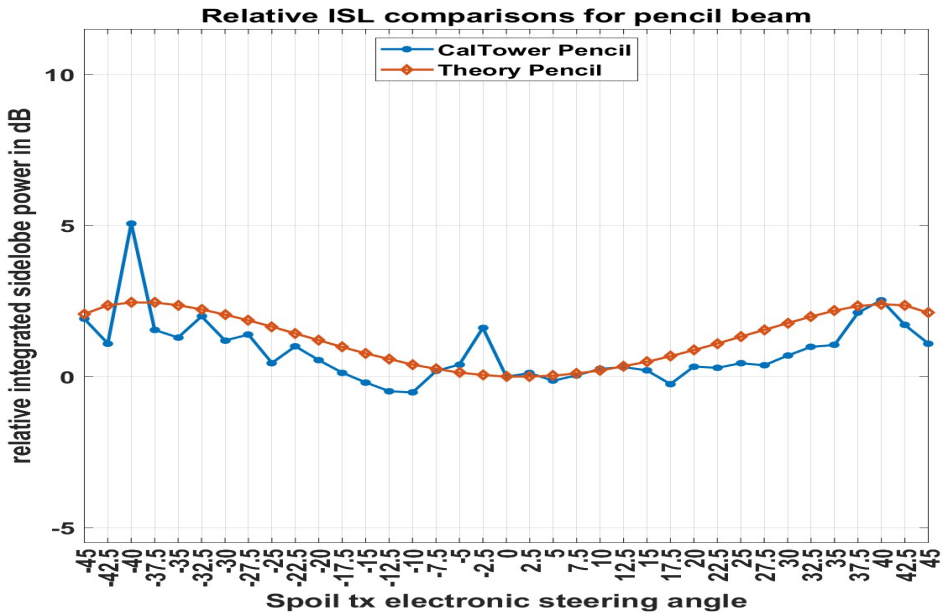

Figure A.7: Relative ISL comparison for pencil beam operations.

Figure A.8: Relative ISL for spoiled beam operations. The central beam plot is expanded for more clarity.

A.5 HPBW

The HPBW metric comparison for pencil beam and spoiled beam operations are shown in Figure A.9.

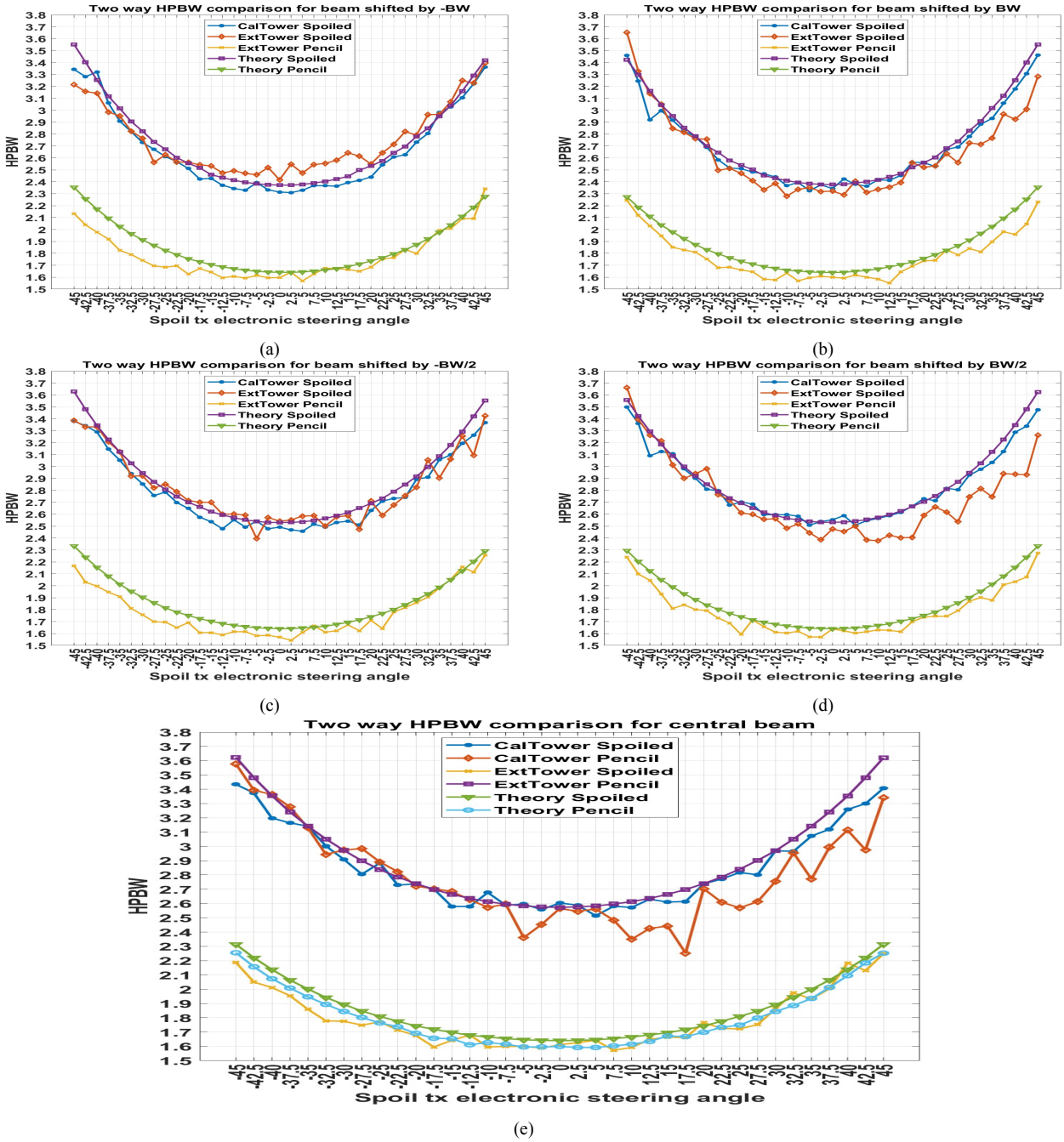

Figure A.9: HPBW comparisons for pencil and spoiled beam operations.

References

Ivić, I. R., 2023: Cross-coupling mitigation in polarimetric par via antenna tilt. Journal of Atmospheric and Oceanic Technology, 40 (5), 587 – 604, https://doi.org/10.1175/JTECH-D-22-0059.1.

Palmer, R., and Coauthors, 2022: A primer on phased array radar technology for the atmospheric sciences. Bulletin of the American Meteorological Society, 103 (10), E2391 – E2416, https://doi.org/10.1175/BAMS-D-21-0172.1.

Schvartzman, D., S. M. Torres, and T.-Y. Yu, 2021: Distributed beams: Concept of operations for polarimetric rotating phased array radar. IEEE Transactions on Geoscience and Remote Sensing, 59 (11), 9173–9191, https://doi.org/10.1109/TGRS.2020.3047090.